Interpreting Summertime Hourly Variation of NO₂ Columns with Implications for Geostationary Satellite Applications

Deepangsu Chatterjee[1], Randall V. Martin[1], Chi Li[1], Dandan Zhang[1], Haihui Zhu[1], Daven K. Henze[2], James H. Crawford[3], Ronald C. Cohen[4,5], Lok N. Lamsal[6], Alexander M. Cede[6]

[1]Department of Energy, Environmental & Chemical Engineering, Washington University in St. Louis, St. Louis, MO, USA
[2]Department of Mechanical Engineering, University of Colorado, Boulder, CO, USA
[3]NASA Langley Research Center, Hampton, VA, USA
[4]Department of Chemistry, University of California, Berkeley, Berkeley, CA, USA
[5]Department of Earth and Planetary Science, University of California, Berkeley, Berkeley, CA, USA
[6]NASA Goddard Space Flight Center, Greenbelt, MD 20771, USA

Correspondence: Deepangsu Chatterjee (deepangsuchatterjee@wustl.edu)

Abstract

Accurate representation of the hourly variation of the NO₂ column-to-surface relationship is needed to interpret geostationary constellation observations of tropospheric NO₂ columns. Prior work has revealed inconsistency in the hourly variation in NO₂ columns and surface concentrations. In this study, we use the high-performance configuration of the GEOS-Chem model (GCHP) to interpret the daytime hourly variation in NO₂ total columns and surface concentrations during summer. We use summer-time Pandora sun photometers and aircraft measurements during the Deriving Information on Surface Conditions from Column and Vertically Resolved Observations Relevant to Air Quality (DISCOVER-AQ) field campaigns over Maryland, Texas, and Colorado as well as 50 sites (31: contiguous USA, 10: Europe, 9: Asia) from the Pandonia Global Network (PGN). We correct the Pandora total NO₂ vertical columns for 1) hourly variation in the column effective temperature driven by the fractional contribution of atmospheric layers to the total NO₂ column, and 2) change in local solar time along the line-of-sight of the Pandora instrument. The corrected Pandora total NO₂ vertical columns are increased by about $5\text{-}6 \times 10^{14}$ molecules cm^{-2} at 9 AM and 6 PM across all Pandora sites. We conduct fine resolution (~12 km) simulations over the contiguous US, Europe, and East Asia using the stretched grid capability of GCHP. We also examine the effect of planetary boundary layer height (PBLH) corrections on the total columns. We first evaluate the GCHP simulated absolute NO₂ concentration with Pandora and aircraft observations. We find that fine resolution simulations at 12 km compared with moderate resolution of ~55 km reduce the Normalized Bias (NB) against Pandora total columns (19% to 10%) and aircraft measurements (25% to 13%) over Maryland, Texas, and Colorado. 12 km simulations also reduce the NB versus Pandora total columns over the eastern US (17% to 9%), western US (22% to 14%), Europe (24% to 15%), and Asia (29% to 21%) as compared to the 55 km simulations. We next use the 12 km simulations to examine the hourly variation in the NO₂ columns and surface concentrations. We explain the weaker hourly variation in NO₂ columns than NO₂ surface concentrations as a function of 1) hourly variation in the column effective temperature, 2) hourly variation in the local solar time along the Pandora line-of-sight, and 3) the differences in hourly variation of atmospheric layers; with the lowest 500 m exhibiting greater NO₂ concentrations in morning and evening than midday, while the residual column above 500 m dominates the total column with weaker variability.

1   Introduction

Nitrogen oxides ($NO_x \equiv NO + NO_2$) affect air quality and human health directly by contributing to premature mortality (Burnett et al., 2004; Tao et al., 2012) and asthma for children and adults (Anenberg et al., 2018), and indirectly by acting as precursors for tropospheric ozone (O_3) formation (Jacob et al., 1996), and nitrate aerosols (Bauer et al., 2007). Significant spatial gaps in ground-based monitoring of surface NO_2 concentrations and pronounced NO_2 heterogeneity inhibit exposure assessment. To fill in the knowledge of NO_2 exposures across a greater fraction of the human population, satellite remote sensing offers the potential for spatially comprehensive measurements. Major advances in satellite remote sensing from sun-synchronous low earth orbit (LEO) has achieved global characterization of tropospheric NO_2 columns at specific times of the day (Duncan et al., 2013; Veefkind et al., 2012) that have been applied to infer ground level NO_2 concentrations (Anenberg et al., 2022; Lamsal et al., 2011; Geddes and Martin, 2017; Cooper et al., 2022). The emerging geostationary constellation (Al-Saadi et al., 2017) including the Geostationary Environmental Monitoring Spectrophotometer (GEMS) over Asia, Tropospheric Emissions: Monitoring Pollution (TEMPO) over North America, and Sentinel-4 over Europe offers the prospect of inferring spatially comprehensive maps of hourly ground-level NO_2 concentrations. Toward this goal, there is a need to develop an accurate representation of the hourly NO_2 column to surface relationship.

Understanding the hourly variation of the relationship of NO_2 columns with surface concentrations is of particular interest due to its role in the inference of hourly surface NO_2 from satellite remote sensing. Numerous studies have separately examined the role of processes such as surface emissions, boundary layer mixing, chemistry, deposition, and advection (Yang et al., 2023b; Herman et al., 2009; Ghude et al., 2020; Zhang et al., 2016) upon the hourly variation of NO_2 columns and upon surface NO_2 concentrations in the United States (Day et al., 2009), Spain

68 (Van Stratum et al., 2012), India (David and Nair, 2011), South Korea (Yang et al., 2023a, b) and

69 China (Tong et al., 2017). Differences have been identified in the daytime hourly variation of NO_2

70 tropospheric columns and surface concentrations during the DISCOVER-AQ and KORUS-AQ

71 (Korea US -Air Quality) campaigns with pronounced variation in surface concentrations that is

72 not evident in the columns (Choi et al., 2020; Crawford et al., 2021). Differences have also been

73 noted in hourly variation of NO_2 measured by aircraft and ground-based Pandora instruments (Li

74 et al., 2021). There is a need to understand the factors that can affect the relationship of hourly

75 NO_2 columns with surface concentrations.

76   Major challenges in the interpretation of satellite NO_2 observations include the short

77 lifetime of NO_x (Laughner and Cohen, 2019), and localized emissions (Crippa et al., 2018) that

78 affect its spatial heterogeneity. Course resolution inputs to satellite retrieval algorithms (e.g.,

79 terrain height, albedo, and a priori NO_2 profiles) can lead to biases (Laughner et al., 2019;

80 Laughner et al., 2018; Russell et al., 2011). Complications with ground-based measurements of

81 the NO_2 columns as part of Pandora include uncertainties at steeper solar zenith angles during

82 morning and evening hours (Herman et al., 2009; Reed et al., 2015) and the changing Pandora

83 field of view (FOV) during morning and late evening (Li et al., 2021). Non-linearities in the

84 relationship between NO_2 concentrations and NO_x sources or sinks can lead to biases in coarse-

85 resolution chemical transport models (CTMs) (Valin et al., 2011) that necessitate CTMs with a

86 finer resolution (Li et al., 2021, 2023a). Recent advances in the simulation of global atmospheric

87 composition at fine resolution (Eastham et al., 2018; Hu et al., 2018; Martin et al., 2022) offer the

88 opportunity to address the resolution need at the global scales of the geostationary constellation.

89   An important consideration in the inference of surface NO_2 concentrations with columnar

90 satellite observations is the vertical profile of NO_2 concentrations. Aircraft observations from the

NASA Deriving Information on Surface Conditions from Column and Vertically Resolved Observations Relevant to Air Quality (DISCOVER-AQ) campaign offers measurements of the NO_2 vertical profile in the lower troposphere for evaluation of modeled vertical profiles (Flynn et al., 2014; Reed et al., 2015). The Pandonia Global Network (PGN) is a global sun photometer network that offers hourly measurements of total NO_2 columns (Verhoelst et al., 2021), useful for interpretation of the daytime variation of NO_2 columns and evaluation of simulated columns. In this study, we interpret the summertime NO_2 measurements from the NASA P-3B aircraft using the high-performance GEOS-Chem (GCHP) simulations along aircraft flight tracks and account for line-of-sight of the Pandora sun photometers over Maryland, Texas, and Colorado during the DISCOVER-AQ campaign. We also explore the effect of vertical changes in the hourly variation of temperature on the NO_2 cross-section and the raw Pandora columns. We further investigate the hourly variation of NO_2 columns and surface concentrations from 50 PGN sites across the northern hemisphere. Section 2 describes the datasets and methods used in this study to interpret the variation of NO_2 columns, surface concentrations, and vertical distribution over DISCOVER-AQ and PGN sites. Section 3 examines the consistency between the NO_2 vertical columns and surface concentrations across DISCOVER-AQ sites, and PGN sites across the contiguous United States (CONUS), Europe, and Asia. We explore the effects of model resolution and boundary layer height adjustments on the hourly variation of NO_2 total columns and surface concentrations as a function of hourly variation in mixed layer depth and photochemistry, and measurement characteristics of Pandora sun photometers over PGN sites across the CONUS, Europe, and Asia.

2   Materials and Methods

2.1   Aircraft measurements of NO_2 vertical profiles

The DISCOVER-AQ campaign offers comprehensive datasets of airborne and surface

114   observations relevant for accessing air quality. One of the main objectives of the campaign was to

115   examine the hourly variation of the relationship between the column and surface concentrations.

116   In this study, we use aircraft, Pandora, and surface measurements over Maryland (July 2011),

117   Texas (September 2013) and Colorado (July-August 2014) to investigate the hourly variation of

118   NO_2 vertical profiles during summer when a long duration of daylight exists for analysis. Figure

119   A1 shows the flight tracks, altitude variation, roadways, and Pandora instrument locations over

120   Maryland, Texas, and Colorado during the DISCOVER-AQ campaign. We focus on the aircraft

121   spirals since they are designed to sample the vertical profile. We use NO_2 concentrations measured

122   by the thermal dissociation laser-induced fluorescence (TD-LIF) technique (Thornton et al., 2000;

123   Day et al., 2002) during the campaign. The laser-induced fluorescence method is highly sensitive

124   for directly measuring NO_2, with a measurement uncertainty of 5 % and a detection limit of 30

125   pptv (Thornton et al., 2000). It also attempts to correct for positive interferences (Nault et al., 2015;

126   Yang et al., 2023b). We use aircraft measurements from a height of about 300 m above ground

127   level (AGL) up to 4 km AGL where high measurement frequency facilitates regional

128   representation.

129   **2.2   Pandonia Global Network NO_2 Total Column Densities**

130   PGN is a global network of ground-based sun photometers that measure sun and sky

131   radiance from 270 to 530 nm that allow retrievals of various trace gases including NO_2. Retrieval

132   precision for total vertical NO_2 columns ("NO_2 columns" hereafter) is 5.4×10^{14} molecules/cm^2

133   with a nominal accuracy of 2.7 x 10^{15} molecules/cm^2 under clear-sky conditions (Herman et al.,

134   2009; Cede 2021). We obtained the level 2 data product from the version rnvs3p1-8 for PGN and

135   DISCOVER-AQ (data source listed in the code and data availability section). We also include

136   surface NO_2 observations from co-located DISCOVER-AQ and PGN sites. We use NO_2 columns

137   and surface concentrations employed during the DISCOVER-AQ campaign from 18 sites over

138   Maryland, Texas and Colorado. We also include NO_2 columns and surface concentrations from 50

139   PGN sites (the US: 31, Europe: 10, Asia: 9) for June-July-August (JJA) 2019. We focus on the

140   NO_2 observations between 9 AM - 6 PM local solar time, for consistency in observation frequency

141   across all PGN sites. Tables A1 and A2 contain the names and locations of the DISCOVER-AQ

142   and PGN sites respectively. We exclude Pandora measurements with SZA>80°. We use total NO_2

143   columns including the stratosphere because the use of external information sources to remove the

144   stratospheric NO_2 columns from PGN can introduce errors in the residual tropospheric columns

145   (Choi et al., 2020).

146   **2.3**   **GEOS-Chem simulations**

147   We use GCHP, the high-performance configuration of the GEOS-Chem model that

148   operates with a distributed-memory framework for massive parallelization (Eastham et al., 2018),

149   to interpret the NO_2 column, vertical distribution and surface observations. GCHP offers the ability

150   to simulate the entire atmospheric column needed to interpret Pandora measurements and the fine

151   spatial resolution needed to interpret aircraft measurements. GEOS-Chem is driven by assimilated

152   meteorological data from the NASA Goddard Earth Observation System (GEOS). GEOS-Chem

153   includes a comprehensive O_x-NO_x-VOC-halogen-aerosol chemical mechanism in the troposphere,

154   in addition to the unified tropospheric-stratospheric chemistry extension in the stratosphere

155   (Eastham et al., 2014). We use GEOS-Chem 14.1.1 which includes recent updates to GCHP

156   (Martin et al., 2022), NO_x heterogenous and cloud chemistry (Holmes et al., 2019), isoprene

157   chemistry (Bates and Jacob, 2019), and aromatic chemistry (Bates et al., 2021). The ISORROPIA

158   II module simulates the thermodynamic partitioning between the gas and condensed phase

159   (Fountoukis and Nenes, 2007). Natural emissions include biogenic volatile organic compounds

160 (VOCs) (Weng et al., 2020), lightning NO_x (Murray et al., 2012), and soil NO_x (Weng et al., 2020).

161 GEOS-Chem includes an updated aircraft NOx emissions inventory for 2019, developed with the

162 Aircraft Emissions Inventory Code (Simone et al., 2013). Figure A2 shows the hourly variation of

163 NO_x emissions across the PGN sites. For the interpretation of PGN measurements in 2019, we

164 conduct the simulations for the year 2019 using GEOS-FP meteorology and the stretched grid

165 capability (Bindle et al., 2021) at a cubed sphere resolution of C180 (~55 km) and stretch factor

166 of 4.0 yielding a regional refinement of ~12 km. All simulations were conducted with a two-week

167 spin-up. We interpolate hourly GCHP outputs of simulated NO_2 columns and surface

168 concentrations to the local solar time at the PGN observation sites.

169   For interpretation of the DISCOVER-AQ aircraft campaigns, we conduct stretched grid

170 simulations over Maryland (July 2011), Texas (September 2013) and Colorado (July-August 2014)

171 with identical stretched grid configurations, with sampling along the aircraft flight tracks. We use

172 MERRA-2 meteorology for these simulations as GEOS-FP meteorology datasets are not available

173 prior to 2014. A sensitivity test for the year 2019 using either GEOS-FP and MERRA-2 affects

174 the local simulated NO_2 columns and surface concentrations by less than 5% for both 12 km and

175 55 km resolutions.

176   Hourly variation of the planetary boundary layer height (PBLH) can influence the vertical

177 distribution and hence the surface concentration of aerosols and trace gases (Lin and McElroy,

178 2010). Millet et al., (2015) found that GEOS-FP reanalysis over-estimates daytime PBLH as

179 compared to observations; correcting for PBLH estimations can lead to a better agreement of ozone

180 (Oak et al., 2019) and $PM_{2.5}$ (Li et al., 2023b) with measurements. Our base case simulation uses

181 the PBLH derived from the Aircraft Meteorological Data Reports (AMDAR) at 54 sites across the

182 CONUS to adjust the PBLH estimates as described in Li et al., (2023). We examine the effect of

183   using the adjusted PBLH for simulations over the CONUS, Europe and East Asia. Table 1 shows

184   the 3 simulation cases conducted over Maryland, Texas, Colorado, the CONUS, Europe and East

185   Asia.

186   Table 1. Summary of GCHP Simulations

187

Name	Description
Base_12	12 km base
NoΔBL_12	12 km without PBLH modification
NoΔBL_55	55 km without PBLH modification

192   **2.5   Effective temperature of Pandora measurements**

193   The NO$_2$ cross section is temperature dependent with the magnitude of spectral features in a 294

194   K NO$_2$ spectrum about 80% of those in 220 K NO$_2$ spectrum (Vandaele et al., 2002). Thus, the

195   NO$_2$ columns fitted with a 220 K NO$_2$ spectrum are about 80% of those fitted with the 294 K NO$_2$

196   spectrum. Prior studies have identified biases in the Pandora total ozone column effective

197   temperature driven by variations in seasonal temperature (Zhao et al., 2016; Herman et al., 2015).

198   To account for the hourly changes in vertical variation of column temperature, we calculate

199   simulated NO$_2$ effective temperatures T_{eff} using the site-specific hourly GEOS-FP temperature

200   profiles $(T)_i$, NO$_2$ cross section $\sigma(NO_2)_i$, and GCHP NO$_2$ vertical profiles $VC(NO_2)_i$ following

201   equation (1) of Herman et al. (2009):

202
$$T_{eff} = \frac{\sum_i^N (\sigma(NO_2)_i \cdot VC(NO_2)_i \cdot (T)_i)}{\sum_i^N (\sigma(NO_2)_i \cdot VC(NO_2)_i)} \tag{1}$$

203   The comparison between GCHP simulated and Pandora observed effective temperature is

204   discussed in sec 3.2.

205 **2.6   Local solar time along Pandora line-of-sight**

206   At observing scenarios with large solar zenith angles, the Pandora sun photometer observes

207   air masses with varying local solar time at different altitudes along the line-of-sight. This feature

208   is particularly noteworthy for comparing hourly Pandora observations with other measurements or

209   simulations. Figure 1 shows the sampling process of GCHP simulations along the line-of-sight of

210   the Pandora sun photometer. GCHP grid boxes are integrated along the viewing geometry of the

211   Pandora instrument to create a "staircase column" that accounts for the effects of local solar time

212   on the horizontal and vertical variation in NO_2 concentrations. The variation in local solar time is

213   most relevant near sunrise and sunset when the NO_2/NOx ratios change rapidly as discussed in

214   section 3.2.   We correct the vertical columns reported by PGN to the local solar time of the

215   instrument by applying the ratio of integrated staircase columns to vertical columns.
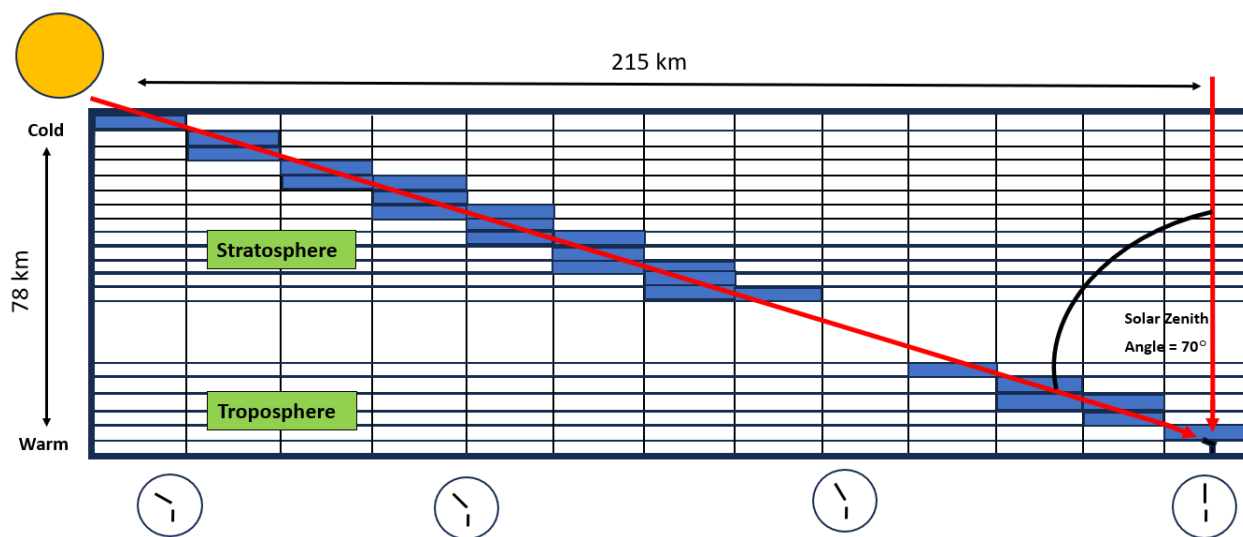
216

217   Figure 1. Configuration of integrating the GCHP grid boxes along the line-of-sight of the Pandora
218   instrument. The shaded grid boxes represent the line-of-sight for the Pandora sun photometer at an inclined
219   solar zenith angle. Clock faces indicate a change in local solar time.

220   **2.7   Ground based surface NO₂ measurements**

221   We use hourly NO_2 surface concentrations from the catalytic converter measurements over

222 DISCOVER-AQ and PGN sites. Based on the approach of Lamsal et al., (2008) and Shah et al.,

223 (2020), we correct the interference of organic nitrates and HNO_3 in the NO_2 measurements, using

224 a correction factor derived from GCHP simulated site-specific NO_2, organic nitrates, and HNO_3

225 mixing ratios. The correction for HNO_3 and organic nitrates reduced the summertime mean NO_2

226 surface concentrations by 18% over DISCOVER-AQ sites and 23% over PGN sites.

227 **2.8   Normalized Bias**

228 We use normalized absolute bias or normalized bias (NB) to evaluate the simulations. The NB is

229 calculated using the following equation-

230
$$NB = \frac{\sum_{i=1}^{N}|S_i - O_i|}{\sum_{i=1}^{N} O_i} \times 100\% \qquad (2)$$

231 where, O_i is the observation and S_i is the corresponding simulated value, i refers to the index of

232 the observation and N refers to the total number of observations.

233 **3   Results and Discussion**

234 **3.1   Hourly variation of observed and simulated NO_2 vertical profiles**

235 Figure 2 shows the hourly variation in the airborne TD-LIF measurements and simulated NO_2

236 vertical profiles at 12 km resolution (Base_12) over Maryland, Texas and Colorado during the

237 DISCOVER-AQ campaign. The measurements exhibit a pronounced maximum at 500 m at 10

238 AM (squares) that diminishes by a factor of 2 in the afternoon as concentrations become more

239 uniform below 1.5 km (triangles and diamonds), driven by the hourly variation in PBLH mixing

240 from early morning to late afternoon. For all three DISCOVER-AQ campaigns, the 12 km

241 simulated NO_2 mixing ratios represent the vertical profile well with normalized bias (NB) below

242 16% at local times: 10 AM, 2 PM, and 5 PM. Differences tend to be larger within 1-2 km above

243 ground level in the afternoon (2 PM and 5 PM local time), which integrates to a lower simulated

244   partial column of 6 x 10^{14} molecules cm^{-2}. The simulated NO_2 vertical profiles at 12 km without

245   PBLH modifications (NoΔBL_12) are similar to those with the PBLH modification (Figure A3).

246   Figure A4 shows the 55 km simulated NO_2 vertical profiles (NoΔBL_55). The 55 km GCHP

247   simulations have increased NB by a factor of 2, as compared to 12 km. Overall, the NO_2 vertical

248   profile exhibits greater consistency with observations at 12 km than at 55 km by better resolving
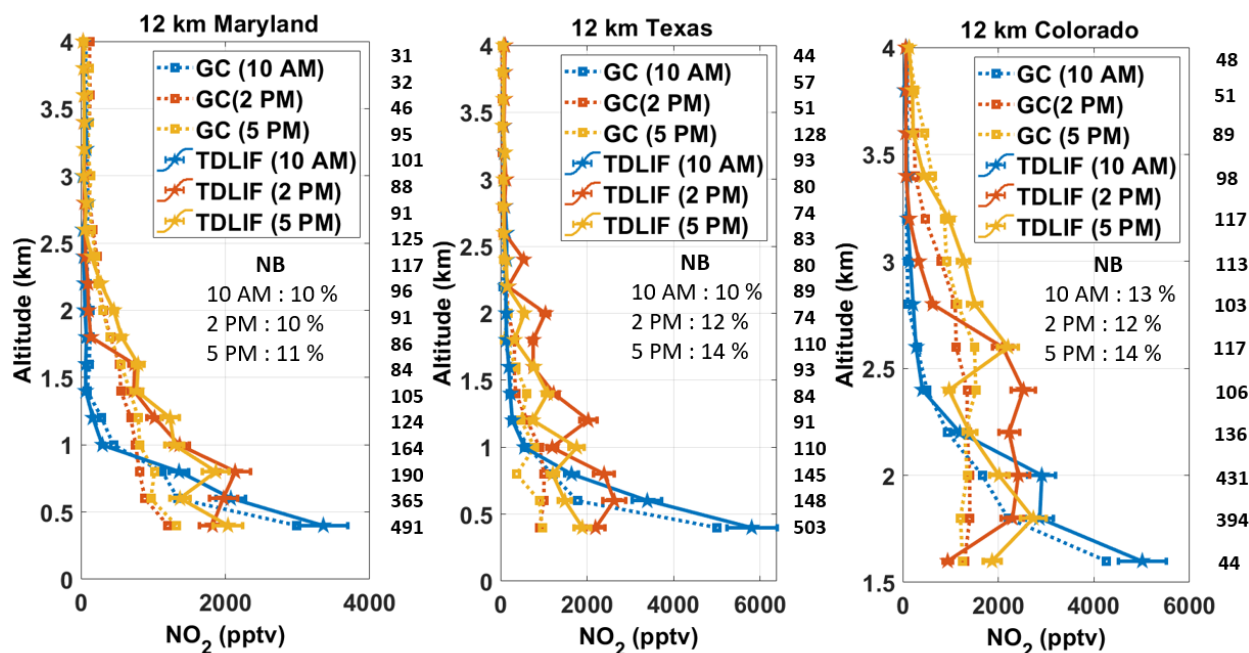
249

250   Figure 2: NO_2 vertical profiles from TD-LIF instrument aboard P-3B during the DISCOVER-AQ campaign
251   over Maryland, Texas, and Colorado. The colored solid lines with pentagram markers represent
252   observations. The dotted colored lines with square markers represent 12 km GCHP simulated mixing ratios.
253   The inset values in the boxes show the normalized biases (NBs) at 10 AM, 2 PM, and 5 PM. The numbers
254   on the right of each panel represent the number the observations associated with the corresponding altitude
255   level. Error bars indicate standard errors in measurements.

256   the heterogeneous conditions along the aircraft flight tracks.

257   **3.2   Corrections to Pandora Effective Temperature**

258   The left panel in Figure 3 shows the Pandora and simulated mean hourly effective temperature of

259   the NO_2 columns over all PGN sites during June-August as inferred using hourly GEOS-FP

260   temperature profiles and GCHP NO_2 vertical profiles. The Pandora effective temperatures exhibit

261 weak hourly variation with a warmer temperature at the Asian sites where boundary layer NO_2

262 concentrations are typically higher than in the US and Europe. The GCHP simulated effective

263 temperature is also warmer for Asian sites, however, the effective temperature is lower during the

264 early afternoon when near-surface NO_2 concentrations tend to be minimum such that the

265 stratospheric NO_2 that makes a larger fractional contribution to the total column. The simulated

266 effective temperature further deviates from the Pandora effective temperature with an increase

267 toward sunrise and sunset with increasing near-surface NO_2 fraction. The corresponding correction
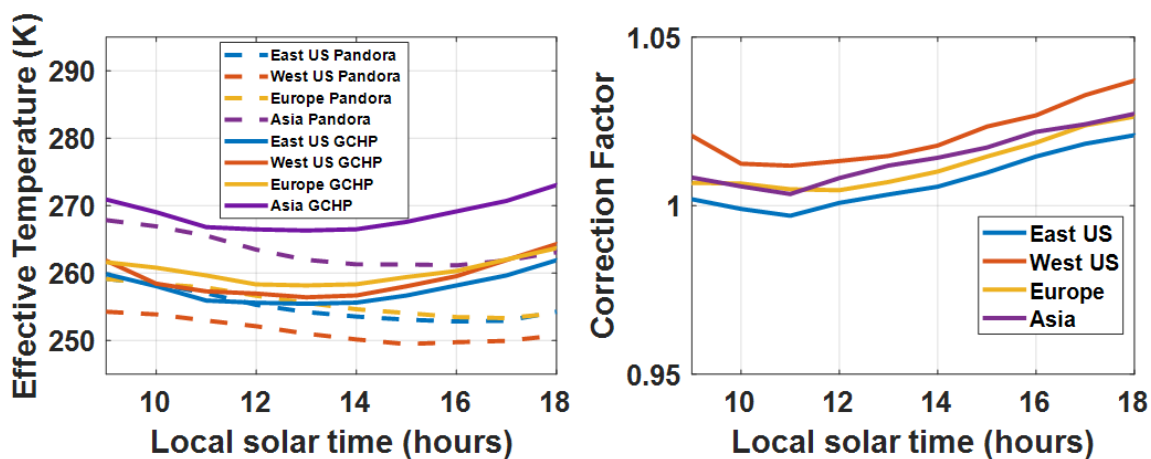
268

269 Figure 3. Hourly variation of the total NO_2 column mean effective temperature across all PGN sites (left
270 panel) and the corresponding correction factors (right panel).

271 factor (CF) for hourly variation in the effective temperature is calculated as:

272
$$CF = 1 + \left(\frac{1}{0.8} - 1\right) \times \frac{(T_{eff}(GCHP(hour)) - T_{eff}(Pandora(hour)))}{294 - 220} \qquad (3)$$

273 The factor of $\left(\frac{1}{0.8} - 1\right)$ reflects the difference between the NO_2 columns fitted with a 220 K NO_2

274 spectrum that are about 80% of those fitted with a 294 K NO_2 spectrum. The CF for the Pandora

275 NO_2 columns increases toward sunrise and sunset due to the increased effective temperature,

276 reflecting the greater abundance of NO_2 molecules observed per unit absorption. We apply site-

277 specific CFs across all Pandora observations.

3.3 Hourly variation of observed and simulated NO₂ VCDs

279   Figure 4 (left) shows the mean hourly daytime Pandora vertical NO_2 columns summarized

280 from the summertime DISCOVER-AQ campaign measurements. The raw Pandora NO_2 columns

281 exhibit weak hourly variation of 8×10^{14} molecules cm^{-2} (within 10% of the daytime mean) that

282 is inconsistent with the aircraft measurements that indicate total columns in the morning and
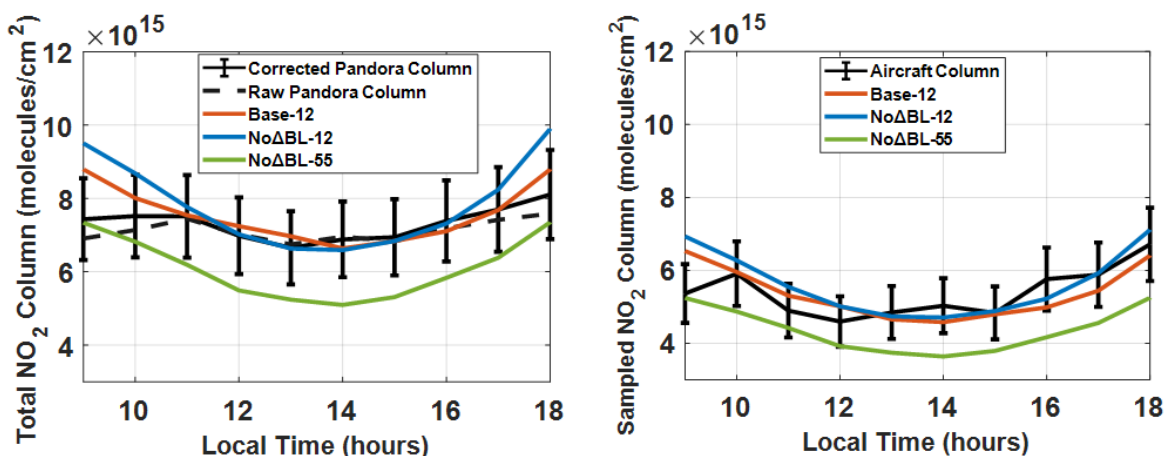
283

284 Figure 4. The left panel shows the total NO_2 vertical columns from corrected DISCOVER-AQ Pandora
285 columns (black), raw DISCOVER-AQ Pandora columns (black dotted), the 12 km base case simulation
286 (red), 12 km without modified PBLH (blue) and 55 km without modified PBLH (green), during the
287 DISCOVER-AQ campaigns over Maryland (2011), Texas (2013) and Colorado (2014). The corrected
288 Pandora columns account for the hourly variation in the effective temperature and the local solar time along
289 the line-of-sight. The right panel shows sampled aircraft and simulated partial columns (300 m A.G.L - 4
290 km A.G.L). Error bars indicate standard error.
291

292 evening of about 1.5×10^{15} molecules cm^{-2} greater than afternoon. The corrected Pandora

293 measurements that account for hourly variation in effective temperature and local solar time along

294 line-of-sight exhibit greater NO_2 columns in morning and evening by about 1.3×10^{15} molecules

295 cm^{-2}, similar to the aircraft measurements. Since the Pandora instruments track the sun, viewing

296 stratospheric air masses 100 - 200 km away from the measurement station to the East in the

297 morning and to the West in the evening, the local solar time of stratospheric NO_2 observed by

298 Pandora instruments near sunrise and sunset is systematically shifted by about 5-10 mins towards

299 noon. This shift can be particularly important during sunrise and sunset when NO_2 columns in the

300 stratosphere undergo a pronounced increase driven by an increasing NO_2/NOx ratio (Figure A5).

301 The 12 km simulated vertical columns generally represent the corrected Pandora observed columns

302 with an NB of 10%. Excluding the PBLH modification would have increased the NB to 13%.

303 Using a coarser 55 km simulation would have further degraded the agreement with an NB of 19%.

304 We sample the GCHP simulated NO_2 columns between 300 m and 4 km to compare with the

305 aircraft columns (right panel). The hourly variation of partial NO_2 columns over 300 m to 4 km

306 AGL from aircraft observations exhibits a distinct increase in morning and evening and are well

307 represented by the 12 km base case simulation (NB = 13%). Similar to our analysis for Pandora

308 sites, excluding the PBLH modification and coarsening the simulation to 55 km degrades the

309 performance (NB = 15% and 25%) versus aircraft columns.

310 Figure 5 extends our analysis to all PGN sites across the CONUS, Europe and East Asia. Raw

311 measurements across all regions exhibit weak hourly variation. The correction for effective

312 temperature and local solar time along the Pandora line-of-site increases the mean NO_2 columns

313 in the morning and evening by about 6×10^{14} molecules cm^{-2} across all regions. The base case

314 simulation generally reproduces measurements with NB of 9% for the eastern US, 14% for the

315 western US, 15% for Europe and 21% for east Asia sites. Excluding the PBLH correction would

316 have increased the NB (eastern US: 12%, western US: 18%, Europe: 18%, and eastern Asia: 26%)

317 with the largest change in Asia. Excluding the PBLH correction yields a higher daytime PBLH

318 resulting in increased chemical lifetime of NO_x, reduced NO_2 dry deposition rates and increased

319 NO_2/NO_x ratio during afternoon and evening (Figure A6), thus leading to an hourly variation that

320 deviates from the Pandora observations. Coarser resolution generally further increases the bias,

321 reflecting resolution effects discussed in the next section. The increase of the simulated total NO_2

322 columns between 3-6 PM across all PGN sites reflects an increase in the NO_2/NO_x ratio throughout

323 the column, driven by a reduction in HO_x (Figure A7).

324
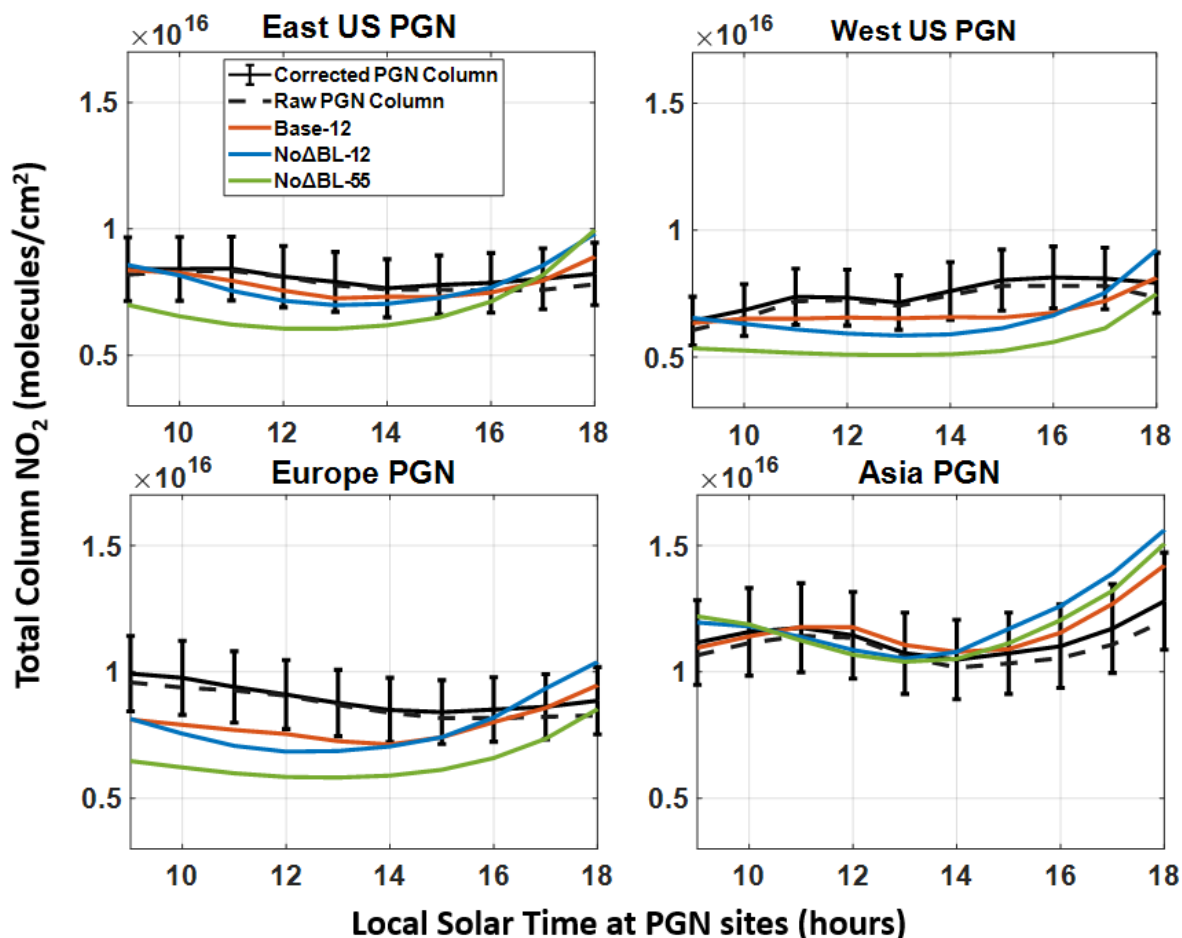
Figure 5. The total NO_2 vertical columns from corrected Pandora columns (black), raw Pandora columns
(black dotted), the 12 km base case simulation (red), 12 km without modified PBLH (blue) and 55 km
without modified PBLH (green) sampled over PGN sites for the summer months of June-July-August in
2019. Error bars indicate standard error.

3.4   Simulated total NO_2 columns

Figure 6 shows the 12 km and 55 km simulated total NO_2 columns, for the summer months of

June-July-August in 2019, between 9 AM and 6 PM (local solar time) over the CONUS. The

overlaid circles show the PGN mean total NO_2 columns. The 12 km simulated NO_2 columns

exhibit greater heterogeneity and better consistency with PGN observed columns (NB = 13%) as

334   compared to the 55 km simulated NO$_2$ columns (NB = 20%). This is primarily driven by better

335   representation of emission and chemical processes at fine resolution (Zhang et al., 2023; Li et al.,

336   2023a). Emissions at these sites are dominated by the transportation sector (Table A3). Figure 7
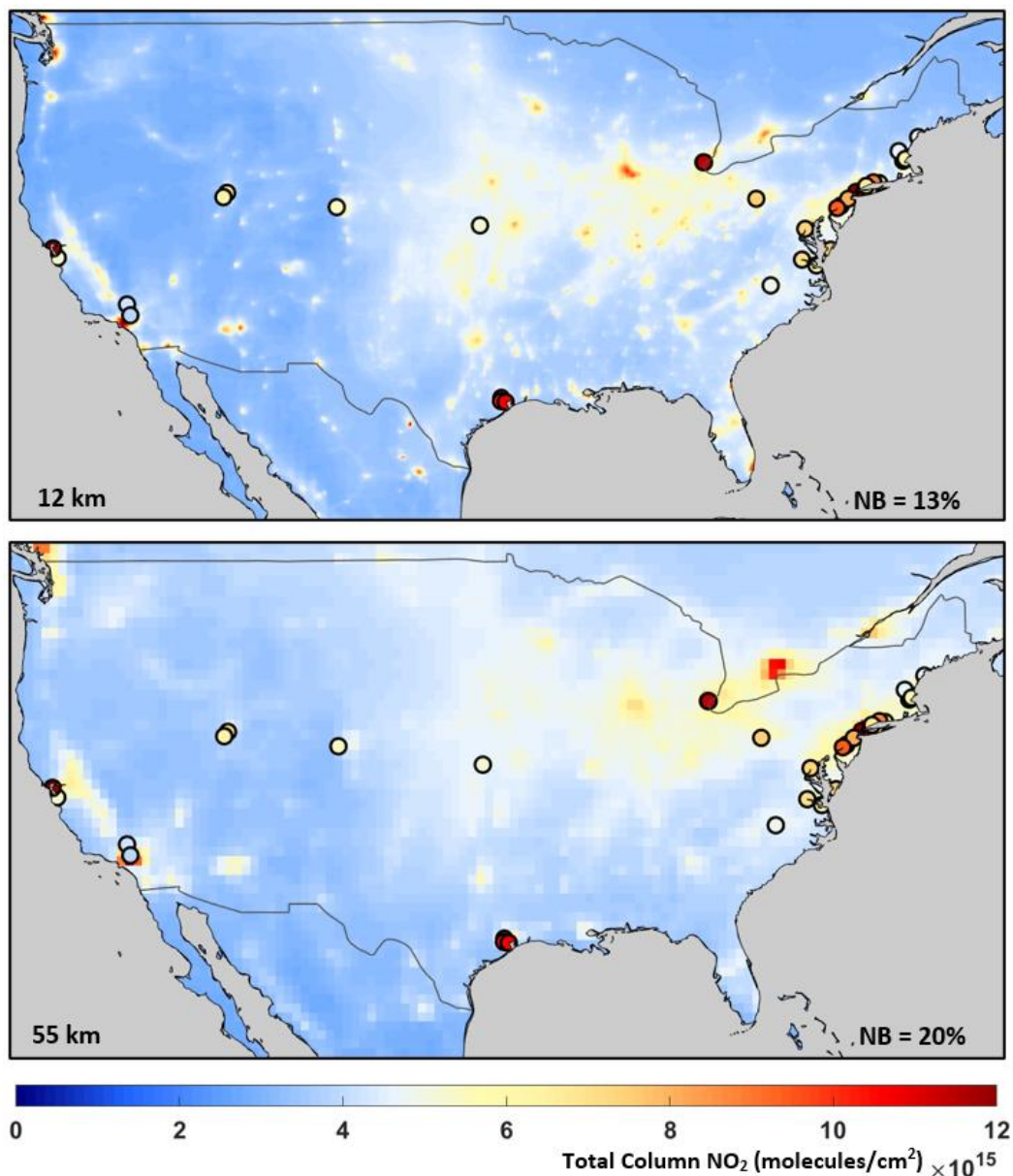
337

338   Figure 6. Simulated NO$_2$ total columns at 12 km (panel A) and 55 km (panel B) horizontal resolutions for
339   the three-month average of June-July-August 2019 over domains where PGN monitors were available
340   between 9 AM – 6 PM local solar time. The solid circles represent the PGN mean total columns between
341   9 AM – 6 PM local solar time for PGN sites in CONUS (31)

342
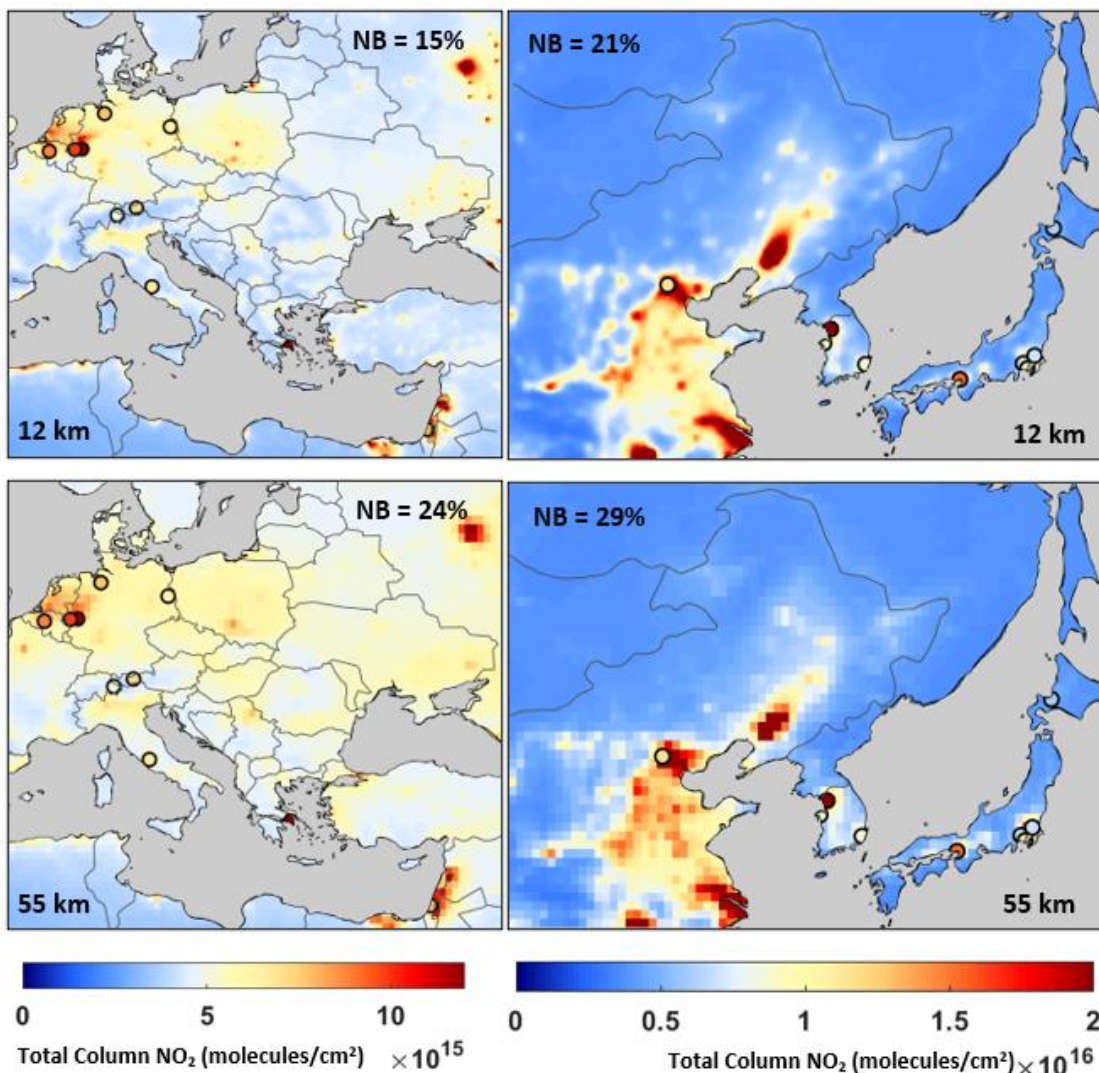
Figure 7. Simulated NO$_2$ total columns at 12 km (panel C and D) and 55 km (panel E and F) horizontal resolutions for the three-month average of June-July-August 2019 over domains where PGN monitors were available between 9 AM – 6 PM local solar time. The solid circles represent the PGN mean total columns between 9 AM – 6 PM local solar time for the PGN sites in Europe (10) and Asia (9).

shows the total NO$_2$ columns from PGN, 12 km simulation and 55 km simulation for the summer

months of June-July- August in 2019, between 9 AM and 6 PM local solar time over Europe and

East Asia. We find enhanced NO$_2$ vertical columns over urban areas in western Europe, eastern

China, Japan and the Korean peninsula. The 12 km simulated NO$_2$ columns exhibit more resolved

combustion features and better agreement with Pandora observed columns for Europe (NB = 15%)

and east Asia (NB = 17%) as compared to the 55 km simulated NO$_2$ columns for Europe (NB =

24%) and east Asia (NB = 29%).

3.5 Hourly variation of observed and simulated surface NO₂ concentrations

Figure 8 shows the hourly variation in surface NO_2 mixing ratios from the corrected in situ

measurements and 12 km simulations over Maryland, Texas and Colorado. Measured NO_2 mixing

ratios are greater in morning and evening than in afternoon as expected from the mixed layer

growth and shorter NO_x lifetime in afternoon. Observed NO_2 surface concentrations over PGN

sites in Asia show enhancement at evening hours (5-6 PM) as compared to PGN sites elsewhere.
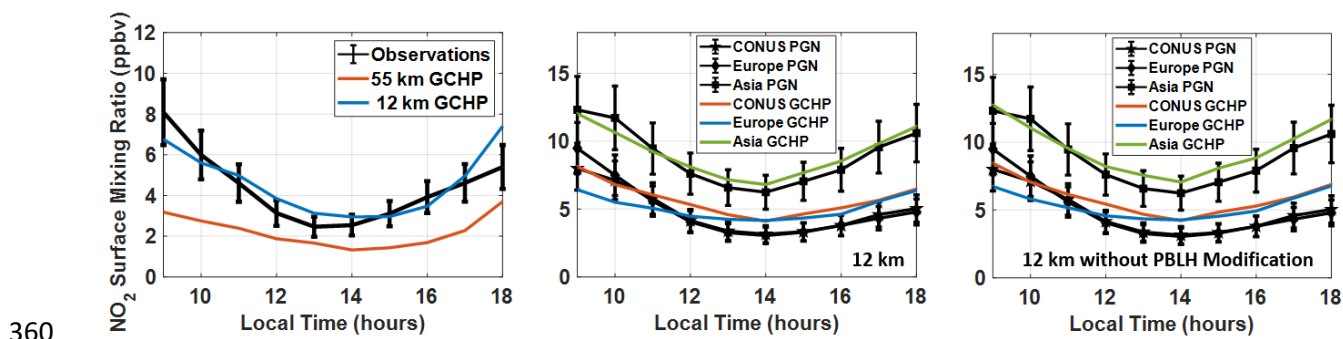
Figure 8. The left panel shows the hourly variation of corrected surface NO_2 mixing ratios from
observations during the DISCOVER-AQ campaign. The middle and right panels show the hourly variation
of observed and 12 km simulated surface NO_2 mixing ratios averaged over the PGN sites with and without
PBLH modification respectively. Error bars indicate standard error.

The measurements are better represented at 12 km (NB = 21%) than at 55 km (NB = 63%) by

better resolving high NO_x emissions near measurement sites. Both Base_12 and NoΔBL_12

simulated NO_2 concentrations generally represent the observations well with NB = 18% (Base_12)

and NB = 20% (NoΔBL_12), across all PGN sites.

3.6 Hourly variation of layer contributions to simulated total NO₂ columns

Given the overall skill of the 12 km simulations in representing the Pandora, aircraft, and surface

NO_2 we proceed to apply the 12 km simulations to understand how the simulated NO_2 vertical

profile affects the simulated NO_2 column to surface relationship. Figure 9 shows the hourly

18

373   variation of simulated contributions to the NO_2 total columns (Base_12) from different vertical

374   layers for multiple regions. In all four regions, within the troposphere, the layer below 0.5 km is

375   the largest contributor at 9 AM with a diminishing contribution into the afternoon associated with

376   mixed layer growth followed by an increasing contribution towards evening. The contribution
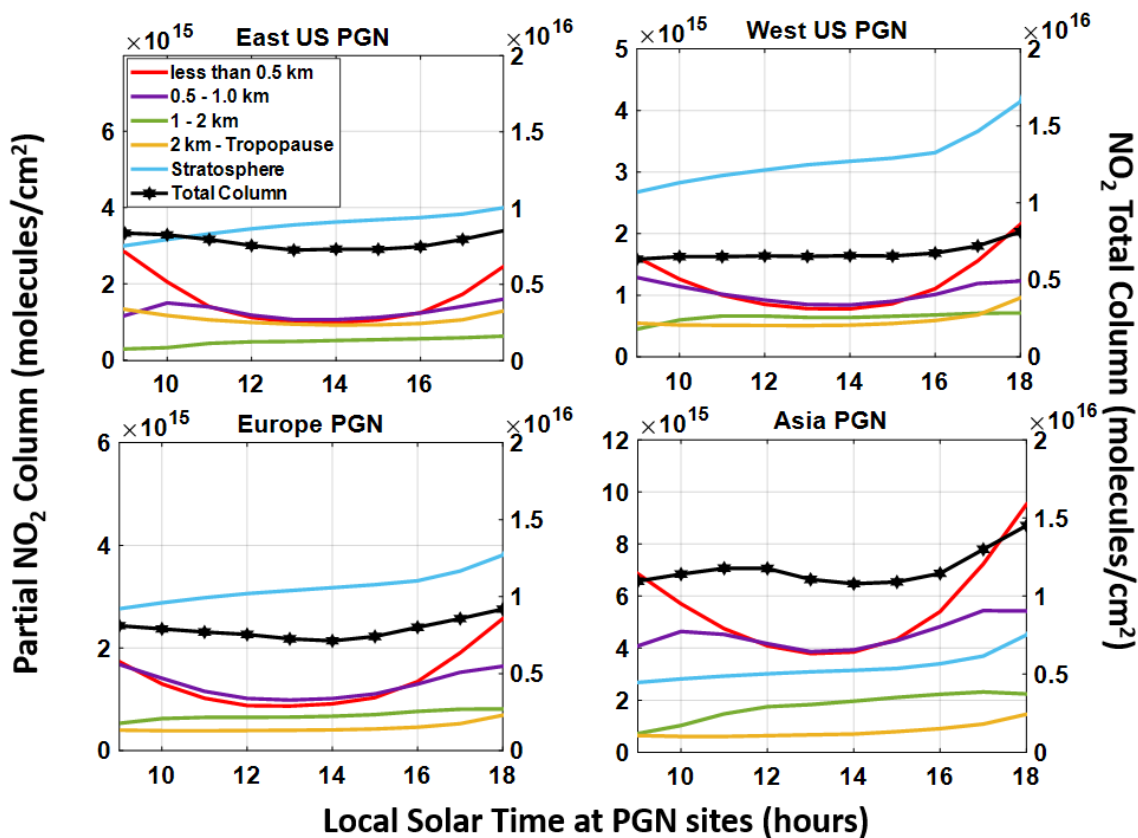
377

378   Figure 9. The simulated absolute contribution of NO_2 columns at different hours of the day averaged over
379   the summer months of June-July-August for 2019 for PGN sites over the eastern US, western US, Europe,
380   and eastern Asia. The colored lines resemble the absolute concentrations from different sections of the
381   column. The black line (hexagon) represents the total NO_2 column. The right y-axis (specifically for the
382   total NO_2 column representing the black marked line) shows the total columns of NO_2.

383   from layers between 0.5 km and the tropopause has weaker variation contributing to the overall

384   weaker variation in total columns. Fractional layer contributions are shown in Figure A8.

385   Fractional hourly variation of the layers above 0.5 km exhibits a compensating inverse behavior,

386   with a pronounced variation in the stratospheric fraction. Contributions from the free troposphere

387   are relatively high for the eastern US reflecting the lightning contribution (Shah et al., 2023; Dang

388 et al., 2023). Over Asia the fractional contribution below 0.5 km is the highest (26% - 42%)

389 reflecting major surface contributions. Overall, we find that for all four regions, the hourly

390 variation in the total column reflects hourly variation below 500 m, dampened by greater column

391 contributions above 500 m that dominate the total column.

392 **Conclusion**

393 We applied GCHP to investigate the hourly variation of summertime NO_2 columns and surface

394 concentrations by interpreting DISCOVER-AQ aircraft and ground-based measurements over

395 Maryland, Texas, Colorado and PGN measurements over the CONUS, Europe, and eastern Asia.

396 We corrected the hourly variation in Pandora observations for the effects of temperature on the

397 NO_2 cross section and the local solar time along the Pandora line-of-sight. The site-specific

398 effective temperature correction factors typically increase the hourly variation of the Pandora

399 observed columns over DISCOVER_AQ sites (3.5% from the daytime mean) and PGN sites (4%

400 from the daytime mean). Near sunrise and sunset, differences in local solar time observed by

401 Pandora in the stratosphere versus the measurement site reflect displacement of 5-10 mins in local

402 solar time toward noon which is relevant in the stratosphere near sunrise and sunset when the

403 NO_2/NO_x ratio is varying rapidly. These corrections to the Pandora measurements improve their

404 consistency with the hourly variation in the NO_2 columns inferred from DISCOVER-AQ aircraft

405 measurements. We find that fine scale simulations at 12 km better represent the NO_2 vertical

406 profile measured by aircraft, reducing the NB from 23% to 16% as compared to simulations at a

407 moderate resolution of 55 km. Simulations at fine resolution (~12 km) of vertical columns along

408 the line-of-sight of Pandora instruments have lower NB with Pandora sun photometers at

409 DISCOVER-AQ sites (10%), and across the eastern US (9%), western US (14%), Europe (15%)

410 and Asia (21%) as compared to moderate resolution (55 km). Fine resolution represents

atmospheric physical and chemical processes with greater accuracy. Excluding the effects of model resolution and the PBLH modification increases the NB to 21% across DISCOVER-AQ sites (over Maryland, Texas and Colorado) and increases the NB at PGN sites over the eastern US (17%), western US (24%), Europe (24%) and east Asia (29%). Adjusting the PBLH to represent observations improves the daytime variation in NO_2/NO_x ratios by increasing the NO_2/NO_x ratio in midday and decreasing the NO_2/NO_x ratio in the afternoon and evening.

Given the overall skill of the 12 km GCHP simulations in representing the corrected Pandora, aircraft, and surface NO_2 measurements, we apply them to derive the hourly contribution of vertical layers to the total tropospheric columns. We find weaker hourly variation in total NO_2 columns than in the lowest 500 m where NO_2 concentrations are greater in morning and evening than midday, while the residual tropospheric column above 500 m dominates the total column with weaker variability. Thus, the weak hourly variation in the column reflects fractional contributions from NO_2 below and above 500 m. Despite the skill of the 12 km simulations in representing the Pandora column measurements, there appears to be greater hourly variation in the simulation, the aircraft measurements, and the surface measurements than in the Pandora observations. Future work should continue to understand this relationship. Future work should also leverage the information developed here to test the performance of surface NO_2 concentrations inferred from the geostationary constellation against ground-based measurements.

Code and Data Availability

GEOS-Chem 14.1.1 along with GCHP code is available for download at https://github.com/geoschem/GCHP.git. The PGN data is available at https://data.pandonia-global-network.org/. The DISCOVER-AQ aircraft and Pandora data are available here:

433 https://asdc.larc.nasa.gov/project/DISCOVER-AQ. For hourly simulated NO₂ datasets please

434 contact the author (deepangsuchatterjee@wustl.edu; deepangsuchatterjee@gmail.com)

Author contributions

436 The manuscript was written using contributions from all authors. The conceptualization was

437 initialized by DC and RVM. The methodology was developed by DC and RVM .DC conducted

438 the model simulations. DC conducted the data analysis with help from CL,DZ,HZ,LL,DH,RC. JC

439 conducted the DISCOVER-AQ campaign. AC manages the PGN datasets. DC and RVM wrote

440 the original draft. All authors have reviewed, edited and given approval to the final version of the

441 manuscript.

Competing interests

443 The contact author has declared that neither they nor their co-authors have any competing interests.

444
445 **Acknowledgments**

446 This work has been supported by the NASA Grant 80NSSC21K1343 and 80NSSC21K0508 and

447 NSF Grant 2244984. We thank the GEOS-Chem support team for maintaining the model used in

448 this work.

449 **Reference**

450 Al-Saadi, J., Kim, J., Lambert, J.-C., Veihelmann, B., and Chance, K.: Geostationary Satellite
451 Constellation for Observing Global Air Quality : Geophysical Validation Needs, 2017.

452 Anenberg, S. C., Henze, D. K., Tinney, V., Kinney, P. L., Raich, W., Fann, N., Malley, C. S., Roman, H.,
453 Lamsal, L., Duncan, B., Martin, R. V., van Donkelaar, A., Brauer, M., Doherty, R., Jonson, J. E., Davila,
454 Y., Sudo, K., and Kuylenstierna, J. C. I.: Estimates of the global burden of ambient PM2:5, ozone, and
455 NO2 on asthma incidence and emergency room visits, Environ. Health Perspect., 126, 1–14,
456 https://doi.org/10.1289/EHP3766, 2018.

457 Anenberg, S. C., Mohegh, A., Goldberg, D. L., Kerr, G. H., Brauer, M., Burkart, K., Hystad, P., Larkin,
458 A., Wozniak, S., and Lamsal, L.: Long-term trends in urban NO2 concentrations and associated paediatric
459 asthma incidence: estimates from global datasets, Lancet Planet. Heal., 6, e49–e58,

460   https://doi.org/10.1016/S2542-5196(21)00255-2, 2022.

461   Bates, K. H. and Jacob, D. J.: A new model mechanism for atmospheric oxidation of isoprene: Global
462   effects on oxidants, nitrogen oxides, organic products, and secondary organic aerosol, Atmos. Chem.
463   Phys., 19, 9613–9640, https://doi.org/10.5194/acp-19-9613-2019, 2019.

464   Bates, K. H., Jacob, D. J., Li, K., Ivatt, P. D., Evans, M. J., Yan, Y., and Lin, J.: Development and
465   evaluation of a new compact mechanism for aromatic oxidation in atmospheric models, Atmos. Chem.
466   Phys., 21, 18351–18374, https://doi.org/10.5194/acp-21-18351-2021, 2021.

467   Bauer, S. E., Koch, D., Unger, N., Metzger, S. M., Shindell, D. T., and Streets, D. G.: Nitrate aerosols
468   today and in 2030: A global simulation including aerosols and tropospheric ozone, Atmos. Chem. Phys.,
469   7, 5043–5059, https://doi.org/10.5194/acp-7-5043-2007, 2007.

470   Belinha, J.: Manual for FEMAS Manual for FEMAS, 1–83, 2016.

471   Bindle, L., Martin, R. V., Cooper, M. J., Lundgren, E. W., Eastham, S. D., Auer, B. M., Clune, T. L.,
472   Weng, H., Lin, J., Murray, L. T., Meng, J., Keller, C. A., Putman, W. M., Pawson, S., and Jacob, D. J.:
473   Grid-stretching capability for the GEOS-Chem 13.0.0 atmospheric chemistry model, Geosci. Model Dev.,
474   14, 5977–5997, https://doi.org/10.5194/GMD-14-5977-2021, 2021.

475   Burnett, R. T., Stieb, D., Brook, J. R., Cakmak, S., Dales, R., Raizenne, M., Vincent, R., and Dann, T.:
476   Associations between Short-Term Changes in Nitrogen Dioxide and Mortality in Canadian Cities, Arch.
477   Environ. Heal. An Int. J., 59, 228–236, https://doi.org/10.3200/AEOH.59.5.228-236, 2004.

478   Cede (2021) https://www.pandonia-global-
479   network.org/wpcontent/uploads/2021/09/BlickSoftwareSuite_Manual_v1-8-4.pdf

480   Choi, S., Lamsal, L. N., Follette-Cook, M., Joiner, J., Krotkov, N. A., Swartz, W. H., Pickering, K. E.,
481   Loughner, C. P., Appel, W., Pfister, G., Saide, P. E., Cohen, R. C., Weinheimer, A. J., and Herman, J. R.:
482   Assessment of NO2 observations during DISCOVER-AQ and KORUS-AQ field campaigns, Atmos.
483   Meas. Tech., 13, 2523–2546, https://doi.org/10.5194/amt-13-2523-2020, 2020.

484   Cooper, M. J., Martin, R. V., Hammer, M. S., Levelt, P. F., Veefkind, P., Lamsal, L. N., Krotkov, N. A.,
485   Brook, J. R., and McLinden, C. A.: Global fine-scale changes in ambient NO2 during COVID-19
486   lockdowns, Nature, 601, 380–387, https://doi.org/10.1038/s41586-021-04229-0, 2022.

487   Crawford, J. H., Ahn, J., Al-saadi, J., Chang, L., Emmons, L. K., Kim, J., Lee, G., Park, J., Park, R. J.,
488   Woo, J. H., Song, C., Hong, J., Hong, Y., Lefer, B. L., Lee, M., Lee, T., Kim, S., Min, K., Yum, S. S.,
489   Shin, H. J., Kim, Y., Choi, J., Park, J., Szykman, J. J., Long, R. W., Jordan, C. E., Simpson, I. J., Fried,
490   A., Dibb, J. E., Cho, S., and Kim, Y. P.: The Korea-United States Air Quality (KORUS-AQ) field study,
491   1–27, 2021.

492   Crippa, M., Guizzardi, D., Muntean, M., Schaaf, E., Dentener, F., Van Aardenne, J. A., Monni, S.,
493   Doering, U., Olivier, J. G. J., Pagliari, V., and Janssens-Maenhout, G.: Gridded emissions of air pollutants
494   for the period 1970-2012 within EDGAR v4.3.2, Earth Syst. Sci. Data, 10, 1987–2013,
495   https://doi.org/10.5194/essd-10-1987-2018, 2018.

496   Dang, R., Jacob, D. J., Shah, V., Eastham, S. D., Fritz, T. M., Mickley, L. J., Liu, T., Wang, Y., and
497   Wang, J.: Background nitrogen dioxide (NO2) over the United States and its implications for satellite
498   observations and trends: effects of nitrate photolysis, aircraft, and open fires, Atmos. Chem. Phys., 23,
499   6271–6284, https://doi.org/10.5194/acp-23-6271-2023, 2023.

500   David, L. M. and Nair, P. R.: Diurnal and seasonal variability of surface ozone and NO x at a tropical
501   coastal site: Association with mesoscale and synoptic meteorological conditions , J. Geophys. Res., 116,
502   1–16, https://doi.org/10.1029/2010jd015076, 2011.

503 Day, D. A., Wooldridge, P. J., Dillon, M. B., Thornton, J. A., and Cohen, R. C.: A thermal dissociation
504 laser-induced fluorescence instrument for in situ detection NO2, peroxy nitrates, alkyl nitrates, and
505 HNO3, J. Geophys. Res. Atmos., 107, https://doi.org/10.1029/2001jd000779, 2002.

506 Day, D. A., Farmer, D. K., Goldstein, A. H., Wooldridge, P. J., Minejima, C., and Cohen, R. C.:
507 Observations of NOx, σpNs, σaNs, and HNO3 at a rural site in the California Sierra Nevada Mountains:
508 Summertime diurnal cycles, Atmos. Chem. Phys., 9, 4879–4896, https://doi.org/10.5194/acp-9-4879-
509 2009, 2009.

510 Duncan, B. N., Yoshida, Y., De Foy, B., Lamsal, L. N., Streets, D. G., Lu, Z., Pickering, K. E., and
511 Krotkov, N. A.: The observed response of Ozone Monitoring Instrument (OMI) NO2 columns to NOx
512 emission controls on power plants in the United States: 2005-2011, Atmos. Environ., 81, 102–111,
513 https://doi.org/10.1016/j.atmosenv.2013.08.068, 2013.

514 Eastham, S. D., Weisenstein, D. K., and Barrett, S. R. H.: Development and evaluation of the unified
515 tropospheric-stratospheric chemistry extension (UCX) for the global chemistry-transport model GEOS-
516 Chem, Atmos. Environ., 89, 52–63, https://doi.org/10.1016/j.atmosenv.2014.02.001, 2014.

517 Eastham, S. D., Long, M. S., Keller, C. A., Lundgren, E., Yantosca, R. M., Zhuang, J., Li, C., Lee, C. J.,
518 Yannetti, M., Auer, B. M., Clune, T. L., Kouatchou, J., Putman, W. M., Thompson, M. A., Trayanov, A.
519 L., Molod, A. M., Martin, R. V., and Jacob, D. J.: GEOS-Chem high performance (GCHP v11-02c): A
520 next-generation implementation of the GEOS-Chem chemical transport model for massively parallel
521 applications, Geosci. Model Dev., 11, 2941–2953, https://doi.org/10.5194/GMD-11-2941-2018, 2018.

522 Flynn, C. M., Pickering, K. E., Crawford, J. H., Lamsal, L., Krotkov, N., Herman, J., Weinheimer, A.,
523 Chen, G., Liu, X., Szykman, J., Tsay, S. C., Loughner, C., Hains, J., Lee, P., Dickerson, R. R., Stehr, J.
524 W., and Brent, L.: Relationship between column-density and surface mixing ratio: Statistical analysis of
525 O3 and NO2 data from the July 2011 Maryland DISCOVER-AQ mission, Atmos. Environ., 92, 429–441,
526 https://doi.org/10.1016/j.atmosenv.2014.04.041, 2014.

527 Fountoukis, C. and Nenes, A.: ISORROPIAII: A computationally efficient thermodynamic equilibrium
528 model for K+-Ca2+-Mg2+-NH4+-Na+-SO42--NO3--Cl--H2O aerosols, Atmos. Chem. Phys., 7, 4639–
529 4659, https://doi.org/10.5194/ACP-7-4639-2007, 2007.

530 Geddes, J. A. and Martin, R. V: Global deposition of total reactive nitrogen oxides from, Atmos. Chem.
531 Phys., 17, 10071–10091, 2017.

532 Ghude, S. D., Karumuri, R. K., Jena, C., Kulkarni, R., Pfister, G. G., Sajjan, V. S., Pithani, P., Debnath,
533 S., Kumar, R., Upendra, B., Kulkarni, S. H., Lal, D. M., Vander A, R. J., and Mahajan, A. S.: What is
534 driving the diurnal variation in tropospheric NO2 columns over a cluster of high emission thermal power
535 plants in India?, Atmos. Environ. X, 5, 100058, https://doi.org/10.1016/j.aeaoa.2019.100058, 2020.

536 Herman, J., Cede, A., Spinei, E., Mount, G., Tzortziou, M., and Abuhassan, N.: NO2 column amounts
537 from ground-based Pandora and MFDOAS spectrometers using the direct-sun DOAS technique:
538 Intercomparisons and application to OMI validation, J. Geophys. Res. Atmos., 114, 1–20,
539 https://doi.org/10.1029/2009jd011848, 2009.

540 Herman, J., Evans, R., Cede, A., Abuhassan, N., Petropavlovskikh, I., and McConville, G.: Comparison
541 of ozone retrievals from the Pandora spectrometer system and Dobson spectrophotometer in Boulder,
542 Colorado, Atmos. Meas. Tech., 8, 3407–3418, https://doi.org/10.5194/amt-8-3407-2015, 2015.

543 Holmes, C. D., Bertram, T. H., Confer, K. L., Graham, K. A., Ronan, A. C., Wirks, C. K., and Shah, V.:
544 The Role of Clouds in the Tropospheric NOx Cycle: A New Modeling Approach for Cloud Chemistry
545 and Its Global Implications, Geophys. Res. Lett., 46, 4980–4990, https://doi.org/10.1029/2019GL081990,
546 2019.

Hu, L., Keller, C. A., Long, M. S., Sherwen, T., Auer, B., Da Silva, A., Nielsen, J. E., Pawson, S., Thompson, M. A., Trayanov, A. L., Travis, K. R., Grange, S. K., Evans, M. J., and Jacob, D. J.: Global simulation of tropospheric chemistry at 12.5 km resolution: Performance and evaluation of the GEOS-Chem chemical module (v10-1) within the NASA GEOS Earth system model (GEOS-5 ESM), Geosci. Model Dev., 11, 4603–4620, https://doi.org/10.5194/gmd-11-4603-2018, 2018.

Jacob, D. J., Heikes, B. G., Fan, S. M., Logan, J. A., Mauzerall, D. L., Bradshaw, J. D., Singh, H. B., Gregory, G. L., Talbot, R. W., Blake, D. R., and Sachse, G. W.: Origin of ozone and NOx in the tropical troposphere: A photochemical analysis of aircraft observations over the South Atlantic basin, J. Geophys. Res. Atmos., 101, 24235–24250, https://doi.org/10.1029/96jd00336, 1996.

L Laughner, J., Zhu, Q., and Cohen, R. C.: Evaluation of version 3.0B of the BEHR OMI NO2 product, Atmos. Meas. Tech., 12, 128–146, https://doi.org/10.5194/amt-12-129-2019, 2019.

Lamsal, L. N., Martin, R. V., van Donkelaar, A., Steinbacher, M., Celarier, E. A., Bucsela, E., Dunlea, E. J., and Pinto, J. P.: Ground-level nitrogen dioxide concentrations inferred from the satellite-borne Ozone Monitoring Instrument, J. Geophys. Res. Atmos., 113, 1–15, https://doi.org/10.1029/2007JD009235, 2008.

Lamsal, L. N., Martin, R. V., Padmanabhan, A., Van Donkelaar, A., Zhang, Q., Sioris, C. E., Chance, K., Kurosu, T. P., and Newchurch, M. J.: Application of satellite observations for timely updates to global anthropogenic NOx emission inventories, Geophys. Res. Lett., 38, https://doi.org/10.1029/2010GL046476, 2011.

Laughner, J. and Cohen, R. C.: Direct observation of changing NO, Science (80-.)., 366, 723–727, 2019.

Laughner, J. L., Zhu, Q., and Cohen, R. C.: The Berkeley High Resolution Tropospheric NO2 product, Earth Syst. Sci. Data, 10, 2069–2095, https://doi.org/10.5194/essd-10-2069-2018, 2018.

Li, C., Martin, R. V., Cohen, R. C., Bindle, L., Zhang, D., Chatterjee, D., Weng, H., and Lin, J.: Variable effects of spatial resolution on modeling of nitrogen oxides, Atmos. Chem. Phys., 23, 3031–3049, https://doi.org/10.5194/acp-23-3031-2023, 2023a.

Li, J., Wang, Y., Zhang, R., Smeltzer, C., Weinheimer, A., Herman, J., Boersma, K. F., Celarier, E. A., Long, R. W., Szykman, J. J., Delgado, R., Thompson, A. M., Knepp, T. N., Lamsal, L. N., Janz, S. J., Kowalewski, M. G., Liu, X., and Nowlan, C. R.: Comprehensive evaluations of diurnal NO2 measurements during DISCOVER-AQ 2011: Effects of resolution-dependent representation of NOx emissions, Atmos. Chem. Phys., 21, 11133–11160, https://doi.org/10.5194/acp-21-11133-2021, 2021.

Li, Y., Martin, R. V., Li, C., Boys, B. L., van Donkelaar, A., Meng, J., and Pierce, J. R.: Development and evaluation of processes affecting simulation of diel fine particulate matter variation in the GEOS-Chem model, Atmos. Chem. Phys., 23, 12525–12543, https://doi.org/10.5194/acp-23-12525-2023, 2023b.

Lin, J. T. and McElroy, M. B.: Impacts of boundary layer mixing on pollutant vertical profiles in the lower troposphere: Implications to satellite remote sensing, Atmos. Environ., 44, 1726–1739, https://doi.org/10.1016/j.atmosenv.2010.02.009, 2010.

GMDD - Improved Advection, Resolution, Performance, and Community Access in the New Generation (Version 13) of the High Performance GEOS-Chem Global Atmospheric Chemistry Model (GCHP): https://gmd.copernicus.org/preprints/gmd-2022-42/, last access: 18 June 2022.

Millet, D. B., Baasandorj, M., Farmer, D. K., Thornton, J. A., Baumann, K., Brophy, P., Chaliyakunnel, S., De Gouw, J. A., Graus, M., Hu, L., Koss, A., Lee, B. H., Lopez-Hilfiker, F. D., Neuman, J. A., Paulot, F., Peischl, J., Pollack, I. B., Ryerson, T. B., Warneke, C., Williams, B. J., and Xu, J.: A large and ubiquitous source of atmospheric formic acid, Atmos. Chem. Phys., 15, 6283–6304,

590 https://doi.org/10.5194/acp-15-6283-2015, 2015.

591 Murray, L. T., Jacob, D. J., Logan, J. A., Hudman, R. C., and Koshak, W. J.: Optimized regional and
592 interannual variability of lightning in a global chemical transport model constrained by LIS/OTD satellite
593 data, J. Geophys. Res. Atmos., 117, 1–14, https://doi.org/10.1029/2012JD017934, 2012.

594 Nault, B. A., Garland, C., Pusede, S. E., Wooldridge, P. J., Ullmann, K., Hall, S. R., and Cohen, R. C.:
595 Measurements of CH3O2NO2 in the upper troposphere, Atmos. Meas. Tech., 8, 987–997,
596 https://doi.org/10.5194/amt-8-987-2015, 2015.

597 Oak, Y. J., Park, R. J., Schroeder, J. R., Crawford, J. H., Blake, D. R., Weinheimer, A. J., Woo, J. H.,
598 Kim, S. W., Yeo, H., Fried, A., Wisthaler, A., and Brune, W. H.: Evaluation of simulated O3 production
599 efficiency during the KORUS-AQ campaign: Implications for anthropogenic NOx emissions in Korea,
600 Elementa, 7, https://doi.org/10.1525/elementa.394, 2019.

601 Reed, A. J., Thompson, A. M., Kollonige, D. E., Martins, D. K., Tzortziou, M. A., Herman, J. R.,
602 Berkoff, T. A., Abuhassan, N. K., and Cede, A.: Effects of local meteorology and aerosols on ozone and
603 nitrogen dioxide retrievals from OMI and pandora spectrometers in Maryland, USA during DISCOVER-
604 AQ 2011, J. Atmos. Chem., 72, 455–482, https://doi.org/10.1007/s10874-013-9254-9, 2015.

605 Russell, A. R., Perring, A. E., Valin, L. C., Bucsela, E. J., Browne, E. C., Wooldridge, P. J., and Cohen,
606 R. C.: A high spatial resolution retrieval of NO2 column densities from OMI: Method and evaluation,
607 Atmos. Chem. Phys., 11, 8543–8554, https://doi.org/10.5194/acp-11-8543-2011, 2011.

608 Shah, V., J. Jacob, D., Li, K., Silvern, R., Zhai, S., Liu, M., Lin, J., and Zhang, Q.: Effect of changing
609 NOx lifetime on the seasonality and long-term trends of satellite-observed tropospheric NO2 columns
610 over China, Atmos. Chem. Phys., 20, 1483–1495, https://doi.org/10.5194/acp-20-1483-2020, 2020.

611 Shah, V., Jacob, D. J., Dang, R., Lamsal, L. N., Strode, S. A., Steenrod, S. D., Boersma, K. F., Eastham,
612 S. D., Fritz, T. M., Thompson, C., Peischl, J., Bourgeois, I., Pollack, I. B., Nault, B. A., Cohen, R. C.,
613 Campuzano-Jost, P., Jimenez, J. L., Andersen, S. T., Carpenter, L. J., Sherwen, T., and Evans, M. J.:
614 Nitrogen oxides in the free troposphere: Implications for tropospheric oxidants and the interpretation of
615 satellite NO2 measurements, Atmos. Chem. Phys., 23, 1227–1257, https://doi.org/10.5194/acp-23-1227-
616 2023, 2023.

617 Simone, N. W., Stettler, M. E. J., and Barrett, S. R. H.: Rapid estimation of global civil aviation emissions
618 with uncertainty quantification, Transp. Res. Part D Transp. Environ., 25, 33–41,
619 https://doi.org/10.1016/j.trd.2013.07.001, 2013.

620 Van Stratum, B. J. H., Vilá-Guerau De Arellano, J., Ouwersloot, H. G., Van Den Dries, K., Van Laar, T.
621 W., Martinez, M., Lelieveld, J., Diesch, J. M., Drewnick, F., Fischer, H., Hosaynali Beygi, Z., Harder, H.,
622 Regelin, E., Sinha, V., Adame, J. A., Sörgel, M., Sander, R., Bozem, H., Song, W., Williams, J., and
623 Yassaa, N.: Case study of the diurnal variability of chemically active species with respect to boundary
624 layer dynamics during DOMINO, Atmos. Chem. Phys., 12, 5329–5341, https://doi.org/10.5194/acp-12-
625 5329-2012, 2012.

626 Tao, Y., Huang, W., Huang, X., Zhong, L., Lu, S. E., Li, Y., Dai, L., Zhang, Y., and Zhu, T.: Estimated
627 acute effects of ambient ozone and nitrogen dioxide on mortality in the Pearl River Delta of southern
628 China, Environ. Health Perspect., 120, 393–398, https://doi.org/10.1289/ehp.1103715, 2012.

629 Thornton, J. A., Wooldridge, P. J., and Cohen, R. C.: Atmospheric NO2: In Situ laser-induced
630 fluorescence detection at parts per trillion mixing ratios, Anal. Chem., 72, 528–539,
631 https://doi.org/10.1021/ac9908905, 2000.

632 Tong, L., Zhang, H., Yu, J., He, M., Xu, N., Zhang, J., Qian, F., Feng, J., and Xiao, H.: Characteristics of

surface ozone and nitrogen oxides at urban, suburban and rural sites in Ningbo, China, Atmos. Res., 187, 57–68, https://doi.org/10.1016/j.atmosres.2016.12.006, 2017.

Valin, L. C., Russell, A. R., Hudman, R. C., and Cohen, R. C.: Effects of model resolution on the interpretation of satellite NO2 observations, Atmos. Chem. Phys., 11, 11647–11655, https://doi.org/10.5194/acp-11-11647-2011, 2011.

Vandaele, A. C., Hermans, C., Fally, S., Carleer, M., Colin, R., Mérienne, M. F., Jenouvrier, A., and Coquart, B.: High-resolution Fourier transform measurement of the NO2 visible and near-infrared absorption cross sections: Temperature and pressure effects, J. Geophys. Res. Atmos., 107, ACH 3-1-ACH 3-12, https://doi.org/10.1029/2001JD000971, 2002.

Veefkind, J. P., Aben, I., McMullan, K., Förster, H., de Vries, J., Otter, G., Claas, J., Eskes, H. J., de Haan, J. F., Kleipool, Q., van Weele, M., Hasekamp, O., Hoogeveen, R., Landgraf, J., Snel, R., Tol, P., Ingmann, P., Voors, R., Kruizinga, B., Vink, R., Visser, H., and Levelt, P. F.: TROPOMI on the ESA Sentinel-5 Precursor: A GMES mission for global observations of the atmospheric composition for climate, air quality and ozone layer applications, Remote Sens. Environ., 120, 70–83, https://doi.org/10.1016/j.rse.2011.09.027, 2012.

Verhoelst, T., Compernolle, S., Pinardi, G., Lambert, J. C., Eskes, H. J., Eichmann, K. U., Fjæraa, A. M., Granville, J., Niemeijer, S., Cede, A., Tiefengraber, M., Hendrick, F., Pazmiño, A., Bais, A., Bazureau, A., Folkert Boersma, K., Bognar, K., Dehn, A., Donner, S., Elokhov, A., Gebetsberger, M., Goutail, F., Grutter De La Mora, M., Gruzdev, A., Gratsea, M., Hansen, G. H., Irie, H., Jepsen, N., Kanaya, Y., Karagkiozidis, D., Kivi, R., Kreher, K., Levelt, P. F., Liu, C., Müller, M., Navarro Comas, M., Piters, A. J. M., Pommereau, J. P., Portafaix, T., Prados-Roman, C., Puentedura, O., Querel, R., Remmers, J., Richter, A., Rimmer, J., Cárdenas, C. R., De Miguel, L. S., Sinyakov, V. P., Stremme, W., Strong, K., Van Roozendael, M., Pepijn Veefkind, J., Wagner, T., Wittrock, F., Yela González, M., and Zehner, C.: Ground-based validation of the Copernicus Sentinel-5P TROPOMI NO2 measurements with the NDACC ZSL-DOAS, MAX-DOAS and Pandonia global networks, Atmos. Meas. Tech., 14, 481–510, https://doi.org/10.5194/amt-14-481-2021, 2021.

Weng, H., Lin, J., Martin, R., Millet, D. B., Jaeglé, L., Ridley, D., Keller, C., Li, C., Du, M., and Meng, J.: Global high-resolution emissions of soil NOx, sea salt aerosols, and biogenic volatile organic compounds, Sci. Data, 7, 1–15, https://doi.org/10.1038/s41597-020-0488-5, 2020.

Yang, L. H., Jacob, D. J., Dang, R., Oak, Y. J., Lin, H., Kim, J., Zhai, S., Colombi, N. K., Pendergrass, D. C., Beaudry, E., Shah, V., Feng, X., Yantosca, R. M., Chong, H., Park, J., Lee, H., Lee, W.-J., Kim, S., Kim, E., Travis, K. R., Crawford, J. H., and Liao, H.: Interpreting GEMS geostationary satellite observations of the diurnal variation of nitrogen dioxide (NO2) over East Asia, EGUsphere, 1–25, 2023a.

Yang, L. H., Jacob, D. J., Colombi, N. K., Zhai, S., Bates, K. H., Shah, V., Beaudry, E., Yantosca, R. M., Lin, H., Brewer, J. F., Chong, H., Travis, K. R., Crawford, J. H., Lamsal, L. N., Koo, J. H., and Kim, J.: Tropospheric NO2vertical profiles over South Korea and their relation to oxidant chemistry: implications for geostationary satellite retrievals and the observation of NO2diurnal variation from space, Atmos. Chem. Phys., 23, 2465–2481, https://doi.org/10.5194/acp-23-2465-2023, 2023b.

Zhang, D., Martin, R. V., Bindle, L., Li, C., Eastham, S. D., van Donkelaar, A., and Gallardo, L.: Advances in Simulating the Global Spatial Heterogeneity of Air Quality and Source Sector Contributions: Insights into the Global South, Environ. Sci. Technol., 57, 6955–6964, https://doi.org/10.1021/acs.est.2c07253, 2023.

Zhang, Y., Wang, Y., Chen, G., Smeltzer, C., Crawford, J., Olson, J., Szykman, J., Weinheimer, A. J., Knapp, D. J., Montzka, D. D., Wisthaler, A., Mikoviny, T., Fried, A., and Diskin, G.: Journal of Geophysical Research : Atmospheres of DISCOVER-AQ 2011 observations, 1–13,

678 https://doi.org/10.1002/2015JD024203.Received, 2016.

679 Zhao, X., Fioletov, V., Cede, A., Davies, J., and Strong, K.: Accuracy, precision, and temperature
680 dependence of Pandora total ozone measurements estimated from a comparison with the Brewer triad in
681 Toronto, Atmos. Meas. Tech., 9, 5747–5761, https://doi.org/10.5194/amt-9-5747-2016, 2016.

682

683

684

685

686

687

688

689

690

691

692

693

694

695

696

697

698

699

700

701

702

703

704

705

706

707

708

Appendix

710

711

712

713
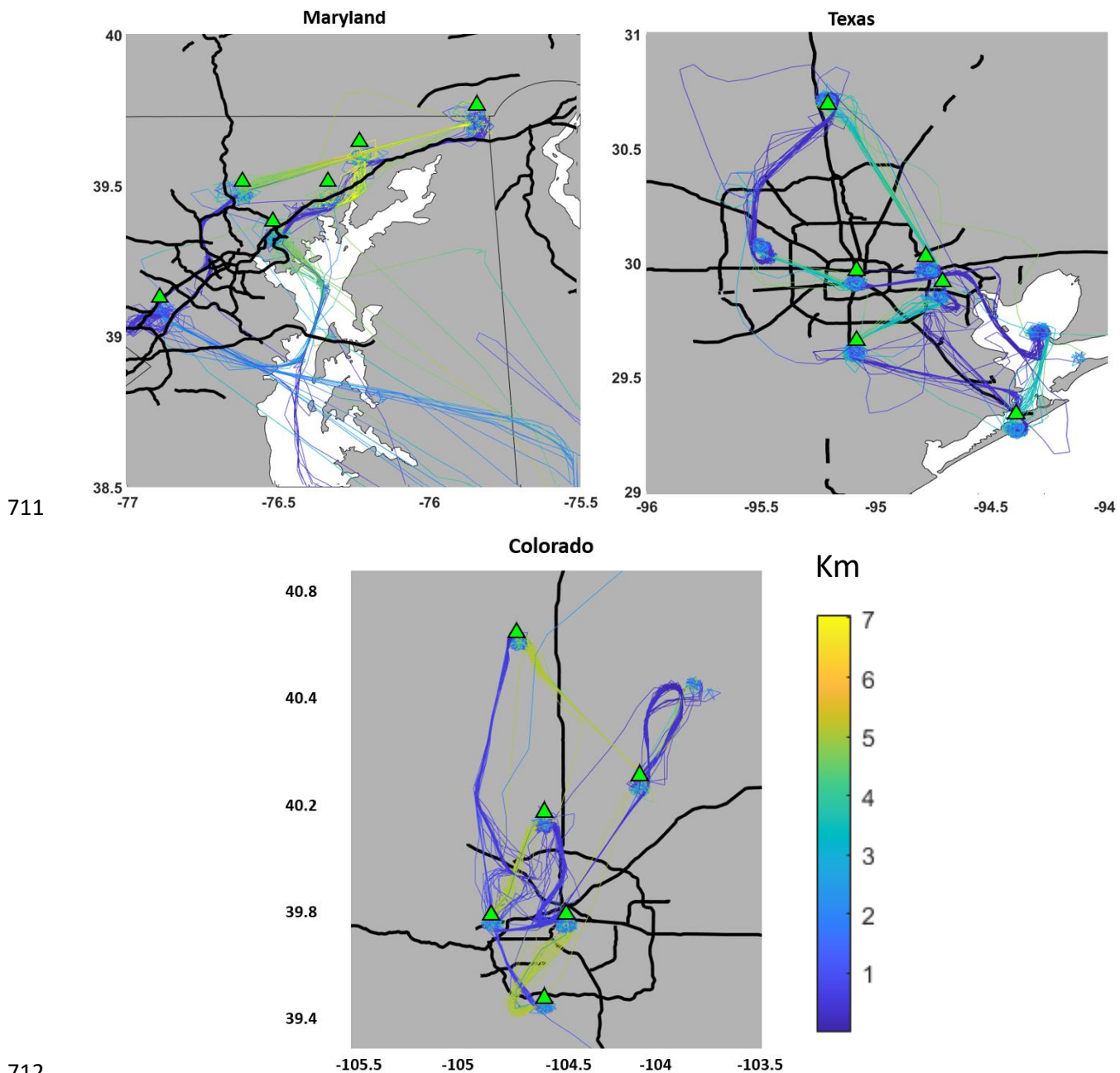
Figure A1. Flight tracks showing the path and altitude of the P-3B aircraft during the DISCOVER-AQ campaign over Maryland during July 2011 (left), over Texas during September 2013 (center) and over Colorado during July-August 2014 (right). The green triangles show the locations of the Pandora sun photometers that have been used in this study. The Sites names and coordinates are listed in Table A1. Grey indicates land, white indicates water. The black bold lines indicate roads.

719
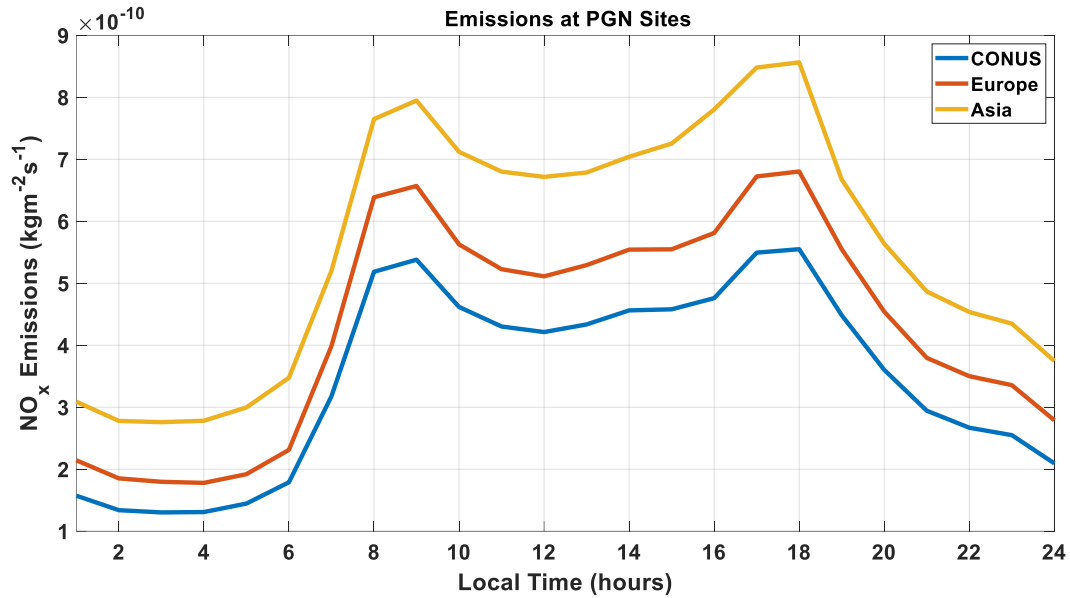
Figure A2. Hourly variation of NOx emissions including all sectors across 50 PGN sites over the CONUS, Europe, and east Asia.

722

723
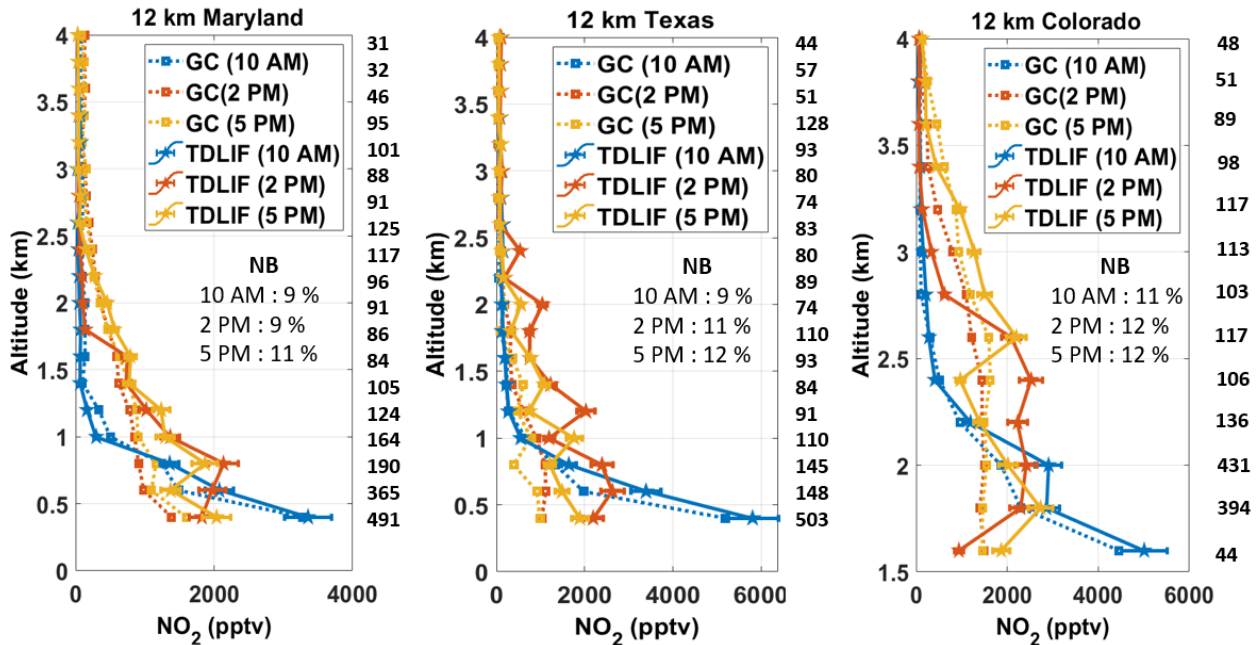
Figure A3: NO_2 Vertical profiles from TD-LIF instrument aboard during the DISCOVER-AQ campaign over Maryland, Texas and Colorado. NO_2 vertical profiles from TD-LIF instrument aboard P-3B during the DISCOVER-AQ campaign over Maryland, Texas and Colorado. The colored solid lines with pentagram markers represent observations .The dotted colored lines with square markers represent 12 km GCHP simulated mixing ratios. The inset values in the boxes show the NB at 10 AM, 2 PM, and 5 PM. The

729 numbers in the middle represent the number the observations associated with the corresponding altitude
730 level. Error bars indicate standard errors in measurements.
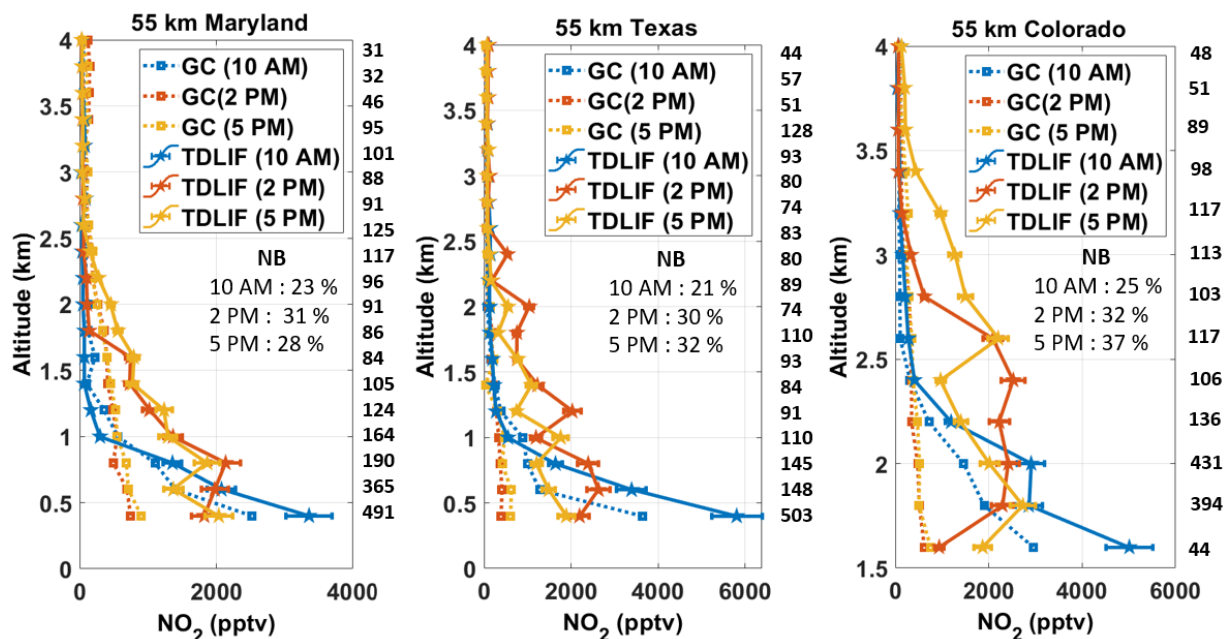
731

732 Figure A4: NO₂ Vertical profiles from TD-LIF instrument aboard during the DISCOVER-AQ campaign
733 over Maryland, Texas and Colorado. NO₂ vertical profiles from TD-LIF instrument aboard P-3B during the
734 DISCOVER-AQ campaign over Maryland, Texas and Colorado. The colored solid lines with pentagram
735 markers represent observations .The dotted colored lines with square markers represent 12 km GCHP
736 simulated mixing ratios. The inset values in the boxes show the NB at 10 AM, 2 PM, and 5 PM. The
737 numbers in the middle represent the number the observations associated with the corresponding altitude
738 level. Error bars indicate standard errors in measurements.

739
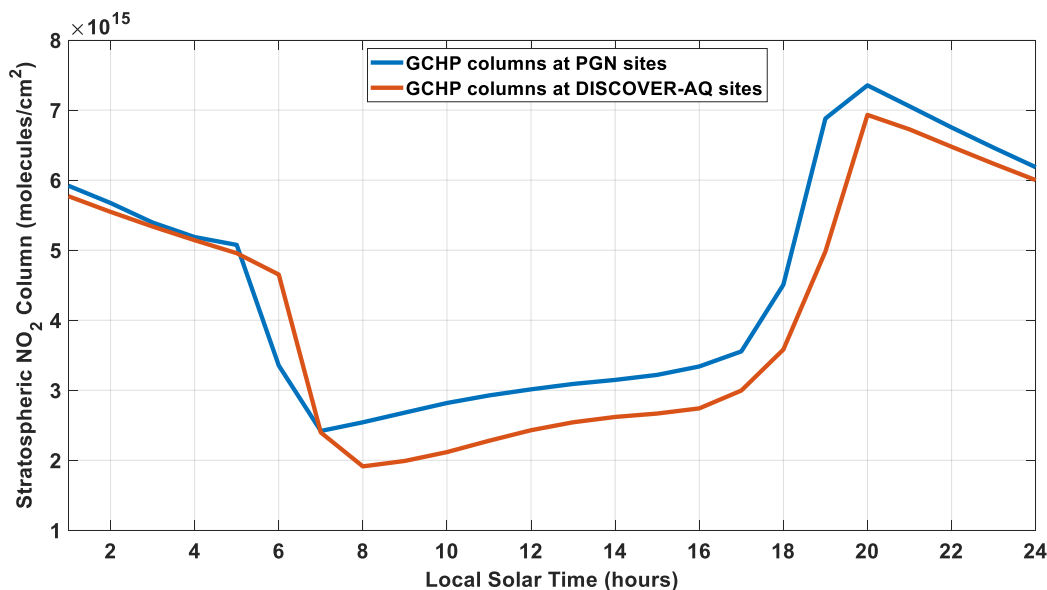
740   Figure A5. GCHP NO$_2$ stratospheric columns for the three-month average of June-July-August at
741   DISCOVER-AQ sites (red) and PGN sites (blue).
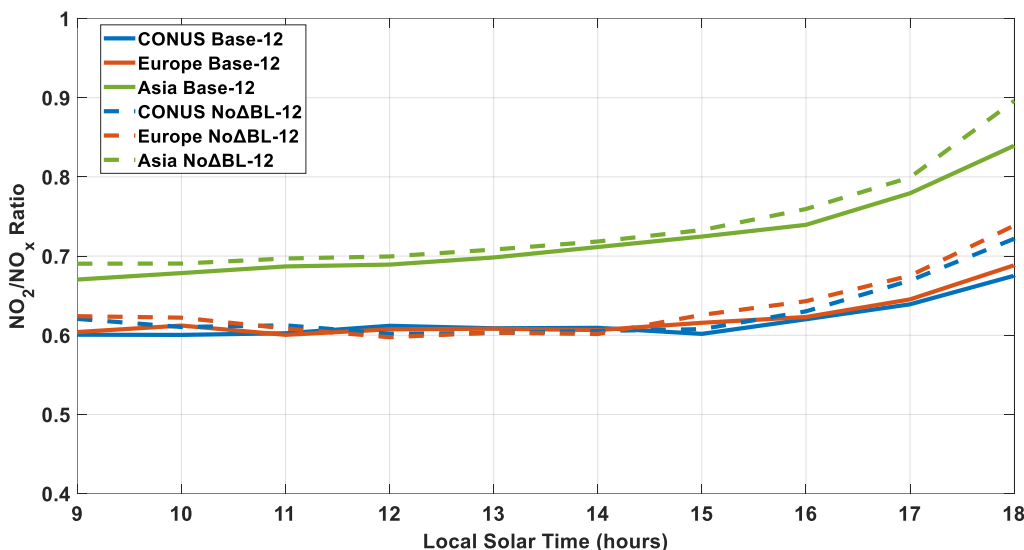
742

743   Figure A6. Hourly variation of 12 km simulated column NO$_2$/NOx ratios across 50 PGN sites over the
744   CONUS (red), Europe (blue), and east Asia (green). The dotted lines show the 12 km simulated NO$_2$/NOx
745   ratios without modified PBLH.

746
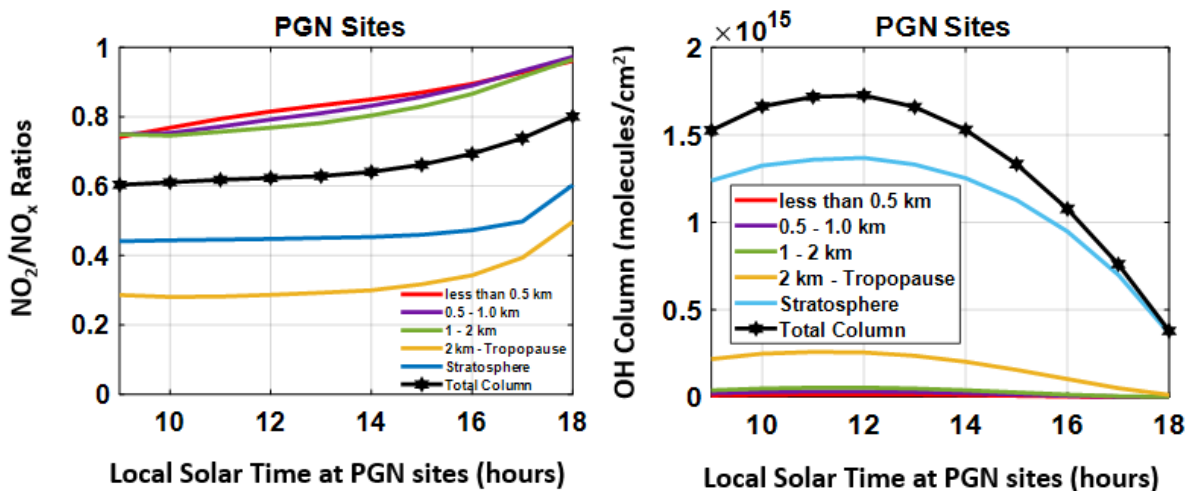
747

748   Figure A7. Simulated NO$_2$/NO$_x$ ratios (left panel) and simulated partial and total OH columns (right panel)
749   at different hours of the day averaged over the summer months of June-July-August for 2019 for PGN sites
750   over the eastern US, western US, Europe, and eastern Asia.
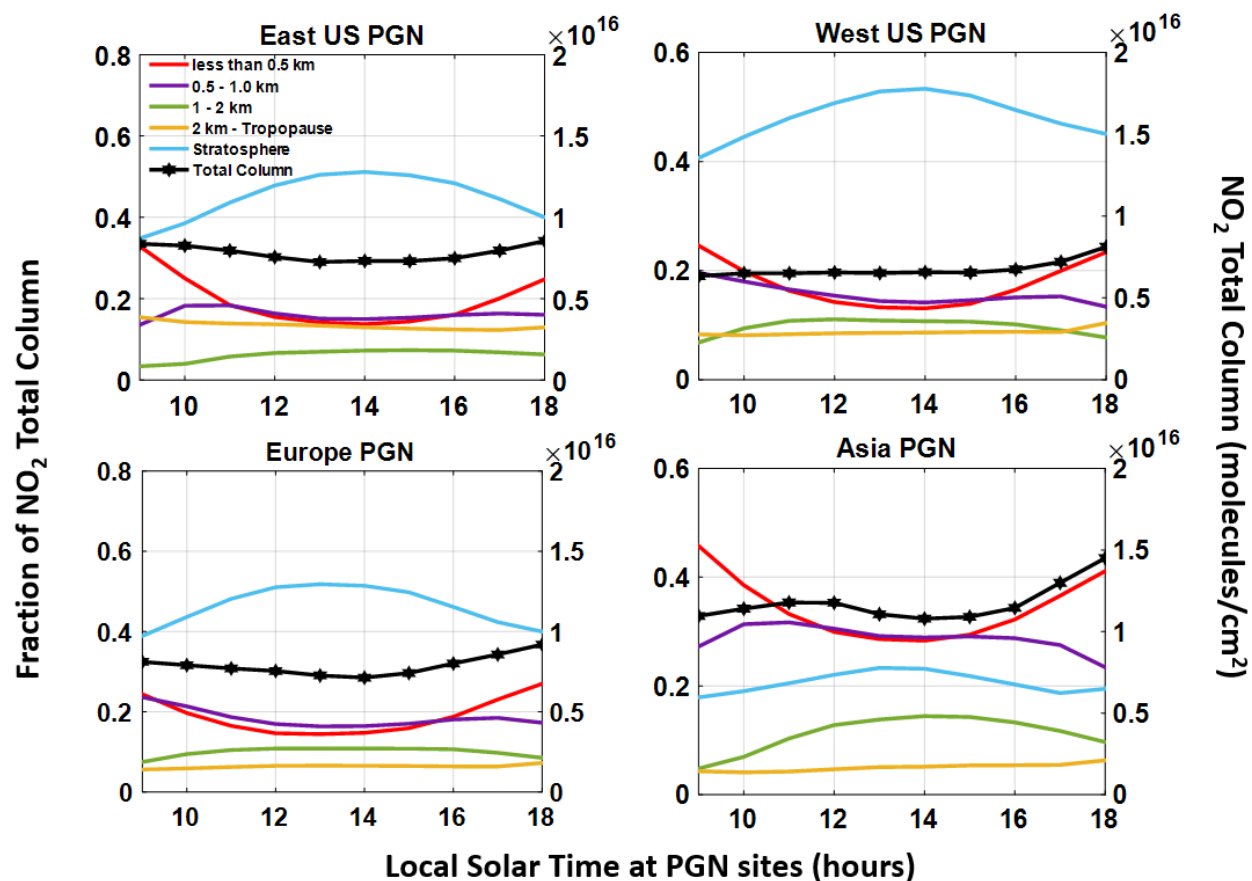
Figure A8. The simulated fractional contribution of NO_2 columns at different hours of the day averaged over the summer months of June-July-August for 2019 for PGN sites over the eastern US, western US, Europe, and eastern Asia. The right Y-axis shows the total columns of NO_2.

Table A1. Site name, latitude and longitude for 18 sites in Texas, Maryland, and Colorado that has concurrent pandora and aircraft measurements.

Site	Sites name	Latitude	Longitude	Date
	Texas Sites			September 2013
1.	Channelview	29.802	-95.125	
2.	Conroe	30.350	-95.425	
3.	Deer Park	29.670	-95.128	
4.	Galveston	29.254	-95.861	
5.	Manvel Croix	29.520	-95.392	
6.	Moody Tower	29.718	-95.341	

766		**Maryland Sites**			July 2011
767	1.	Aldino	39.563	-76.204	
768	2.	Beltsville	39.055	-76.878	
769	3.	Edgewood	39.410	-76.297	
770	4.	Essex	39.311	-76.474	
771	5.	Fairhill	39.701	-75.860	
772	6.	Padonia	39.461	-76.631	
773		**Colorado Sites**			July-August 2014
774	1.	Bao Tower	40.043	-105.012	
775	2.	Chatfield Park	39.535	-105.074	
776	3.	Denver La Casa	39.782	-105.018	
777	4.	Fort Collins	40.595	-105.143	
778	5.	Platteville	40.183	-104.734	
779	6.	NREL-Golden	39.743	-105.181	

780

781 Table A2. Site name, latitude and longitude for 31 sites in CONUS and 11 sites in Europe, North

782 Africa and Middle-east, and 9 sites in east Asia from the PGN database.

783

Site	Site Name	Latitude	Longitude	Date
	Eastern US			June-July-August 2019
1.	'Bristol_PA'	40.1074	-74.8824	
2.	'Cambridge_MA'	42.3800	-71.1100	
3.	'CapeElizabeth_ME'	43.5610	-70.2073	
4.	'ChapelHill_NC'	35.9708	-79.0933	
5.	'CharlesCity_VA'	37.3260	-77.2057	
6.	'Dearborn_MI'	42.3067	-83.1488	

7.	'Detroit_MI.txt'	42.3026	-83.1068
8.	'Hampton_VA'	37.0203	-76.3366
9.	'Londonderry_NH'	42.8625	-71.3801
10.	'Lynn_MA'	42.4746	-70.9708
11.	'Madison_CT'	41.2568	-72.5533
12.	'Manhattan_NY'	40.8153	-73.9505
13.	'NewBrunswick_NJ'	40.4622	-74.4294
14.	'NewHaven_CT'	41.3014	-72.9029
15.	'OldField_NY'	40.9635	-73.1402
16.	'Philadelphia_PA'	39.9919	-75.0811
17.	'Pittsburgh_PA '	40.4655	-79.9608
18.	'WallopsIsland_VA '	37.8439	-75.4775
19.	'WashingtonDC'	38.9218	-77.0124
20.	'Westport_CT'	41.1183	-73.3367

Western US   June-July-August 2019

21.	'Aldine_TX'	29.9011	-95.3262
22.	'Boulder_CO'	40.0375	-105.2420
23.	'Edwards_CA '	34.9600	-117.8811
24.	'Houston_TX'	29.7200	-95.3400
25.	'LaPorte_TX'	29.6721	-95.0647
26.	'Manhattan_KS'	39.1022	-96.6096
27.	'MountainView_CA'	37.4200	-122.05680
28.	'Richmond_CA'	37.9130	-122.3360

29.	'SaltLakeCity_UT'	40.7663	-111.8478
30.	'SouthJordan_UT'	40.5480	-112.0700
31.	'Wrightwood_CA'	34.3819	-117.6813

	Europe			June-July-August 2019
32.	'Athens'	37.9878	23.7750	
33.	'Bremen'	53.0813	8.8126	
34.	'Brussels'	50.7980	4.3580	
35.	'Cologne'	50.9389	6.9787	
36.	'Davos'	46.8000	9.8300	
37.	'Innsbruck'	47.2643	11.3852	
38.	'Juelich'	50.9080	6.4130	
39.	'Lindenberg'	52.2900	14.1200	
40.	'Rome'	42.1057	12.6402	
41.	'Tel-Aviv'	32.1129	34.8062	

	Eastern Asia			June-July-August 2019
42.	'Beijing'	40.0048	116.3786	
43.	'Kobe'	34.7190	135.2900	
44.	'Sapporo'	43.0727	141.3459	
45.	'Seosan'	36.7769	126.4938	
46.	'Seoul'	37.5644	126.9340	
47.	'Tokyo'	35.6200	139.3834	
48.	'Tsukuba'	36.0661	140.1244	

| 49. | 'Ulsan' | 35.5745 | 129.1896 |
| 50. | 'Yokosuka' | 35.3207 | 139.6508 |

784 ____

785 Table A3. Sectoral contribution to NOx emissions averaged over all PGN sites, the US, Europe
786 and Asia.

PGN Sites	TRA(%)	RCO(%)	IND(%)	ENE(%)	SHP(%)	AGR(%)	WST(%)
ALL	49	19	13	7	7	4	1
CONUS	45	29	16	4	2	3	1
Europe	47	11	8	10	16	7	1
Asia	55	12	15	9	4	3	2

787

788 TRA: Transport, RCO: Residential Combustion, IND: Industry, ENE: Energy, SHP: Ship Emissions, AGR:
789 Agriculture, WST: Waste

790